Comparison of the wake recovery of the axial-flow and cross-flow turbine concepts

Matthieu Boudreau[a], Guy Dumas[b*]

CFD Laboratory LMFN, Département de génie mécanique, Université Laval,
1065 avenue de la Médecine, Québec, Qc, Canada, G1V 0A6
[a] *matthieu.boudreau.1@ulaval.ca*
[b] *gdumas@gmc.ulaval.ca*

Postprint, 2017 - Journal of Wind Engineering and Industrial Aerodynamics
Published version available online at: https://doi.org/10.1016/j.jweia.2017.03.010

Abstract

A detailed wake analysis of two different turbine concepts is conducted to gain a fundamental understanding of the main energy recovery processes at play in each case. An axial-flow turbine and a cross-flow turbine are considered. Both operate near their respective optimal efficiency conditions in a uniform oncoming flow and at a Reynolds number of 10^7. Three-dimensional Delayed Detached-Eddy Simulations (DDES) are carried out and the time-averaged Unsteady Reynolds-averaged Navier-Stokes (URANS) equations are used as a post-processing tool in order to assess the importance of the various contributions affecting the wake recovery quantitatively. It is found that the dominant mechanism is fundamentally different between the two turbine technologies. Indeed, while the axial-flow turbine's wake is strongly influenced by an instability phenomenon leading to a significant turbulent transport, the cross-flow turbine's wake recovery is found to be much more related to the mean spanwise velocity field. As a result, unlike the axial-flow turbine's wake dynamics which is highly dependent on the turbulent characteristics of the oncoming flow, the cross-flow turbine's wake is expected to be less sensitive to these turbulent characteristics but highly dependent on the geometric characteristics of the turbine such as the turbine's aspect ratio.

Keywords: Wind turbine, hydrokinetic turbine, axial-flow, cross-flow, wake, vortex dynamics

1. Introduction

Renewable energy sources, such as marine currents and winds, are diffuse compared to the energy coming from fossil fuels (Lago et al., 2010). Consequently, it is critical to densify the energy production of hydrokinetic and wind turbines by suitably placing them in farms for this energy sector to become economically competitive. In this context, the choice of a particular technology over another does not depend solely on the efficiency of a single machine but the interactions between the turbines must also be taken into account (Dabiri, 2011). Moreover, it has been found that, for very large turbine farms (several turbine rows), the amount of energy available for each turbine strongly depends on the vertical kinetic energy fluxes ($-\rho\, U_\infty\, (\overline{u'\, w'})$) from the flow passing above the turbines to the flow at the turbines' level (Abkar & Porté-Agel, 2014; Calaf et al., 2010; Chamorro et al., 2011). In an infinitely long turbine farm, these vertical energy fluxes necessarily balance the power extracted by the turbines. Since these fluxes are affected by the flow topology in the turbines' wakes, it is important to characterize the wake dynamics of different types of turbine, such as the axial-flow turbine (AFT) and the cross-flow turbine (CFT), as a specific turbine could become interesting in the context of a very large turbine farm even if it is not the most efficient one when it is considered individually, in isolation. It is also worth mentioning that some recent findings have shown that a turbine's farm performance could be increased by operating the turbines at non-optimum conditions Kazda et al. (2016), therefore again demonstrating that the performances of turbines in isolation are not the only parameters of interest when optimizing a farm.

Several studies have been devoted to the analysis of the flow field in the wake of a single axial-flow turbine, with some of them focusing on the tip vortices' dynamics in the near wake (Chamorro et al., 2013b; Lignarolo et al., 2014; Zhang et al., 2012). Sherry et al. (2013) performed PIV measurements in the wake of an AFT facing a uniform oncoming flow and focused on the vortex instability occurring in the wake, which was found to be strongly dependent on the tip speed ratio. Lignarolo et al. (2014) minimized the ambient turbulence in their experimental facilities and their stereoscopic particle image velocimetry (SPIV) measurements have suggested that the enhanced mixing caused by the tip vortices' instability has a pronounced effect on the momentum recovery. However, their measurements were limited to the near wake, i.e., up to only 5 diameters downstream of the turbine, and they did not quantify the relative contribution of the tip vortices' instability in comparison with the other mechanisms affecting the momentum recovery.

Owing to the fact that the AFT's wake dynamics is highly influenced by the turbulent characteristics of the oncoming flow (Chamorro & Porté-Agel, 2009; Chu & Chiang, 2014; Mycek et al., 2014a,b; Zhang et al., 2012) and in order to

*Corresponding author
Email address: gdumas@gmc.ulaval.ca (Guy Dumas[b])

be as faithful as possible to realistic turbine operating conditions, several recent AFT wake studies have been performed on turbines operating in a turbulent boundary layer (Cal et al., 2010; Chamorro & Porté-Agel, 2009, 2010; Chamorro et al., 2013a,b; El-Askary et al., 2017; Hu et al., 2012; Porté-Agel et al., 2011; Wu & Porté-Agel, 2012; Zhang et al., 2012), either corresponding to the atmospheric boundary layer in the case of wind turbines or to the marine boundary layer in the case of hydrokinetic turbines. Among these studies, it is worth mentioning that Chamorro et al. (2013b) and Zhang et al. (2012) performed, respectively, detailed particle image velocimetry (PIV) and volumetric 3-component velocimetry (V3V) measurements of the three velocity components and the Reynolds stresses in an axial-flow turbine's near wake. Chamorro et al. (2012b) and Wu & Porté-Agel (2012) evaluated various terms of the turbulent kinetic energy budget in the wake of an axial-flow turbine operating in a boundary layer flow through experimental measurements and numerical simulations. A few works have also been devoted to the study of the energy transport in AFT arrays by carrying out a budget of either the mean kinetic energy equation (Abkar & Porté-Agel, 2014; Cal et al., 2010; Hamilton et al., 2012; Lebron et al., 2012; Newman et al., 2014; VerHulst & Meneveau, 2014) or the turbulent kinetic energy equation (Abkar & Porté-Agel, 2014). These studies have highlighted the importance of the radial turbulent transport in axial-flow turbines' wakes. Furthermore, Meyers & Meneveau (2013) visualized the energy transport in various configurations of turbine arrays using the concept of the energy transport tube. Lastly, the interested reader is referred to two recent reviews discussing the flow topology in axial-flow turbines' farms (Mehta et al., 2014; Stevens & Meneveau, 2017).

Regarding the cross-flow turbine concept, numerous experimental measurements have been taken in the wake of the straight-blade H-Darrieus turbine concept (Bachant & Wosnik, 2013, 2015, 2016; Battisti et al., 2011; Brochier et al., 1986; Hofemann et al., 2008; Ryan et al., 2016; Simão Ferreira et al., 2006, 2007, 2009, 2010; Tescione et al., 2014). Battisti et al. (2011) performed hot-wire measurements on a plane normal to the upstream flow located 1.5 diameters downstream of such a CFT in open and closed wind tunnel configurations. They presented time-averaged and phase-averaged results and showed the importance of the tip effects on the turbine's performances and on its wake topology. Other studies focused on the evolution of the shed vorticity and the tip vortices in the wake of the H-Darrieus turbine and highlighted the fact that the tip vortices ejected from the CFT blades tend to convect toward the wake center in the spanwise direction (Hofemann et al., 2008; Simão Ferreira et al., 2006, 2007, 2009, 2010; Scheurich et al., 2011). The same observation was also made more recently by Tescione et al. (2014) who used the PIV technique to observe in details the flow field in the near wake of an H-Darrieus CFT turbine. However, their measurements only covered the first three diameters downstream of the turbine's axis of rotation. Measurements up to seven and ten diameters downstream have been taken by Ryan et al. (2016), who showed the effects of the tip speed ratio on the wake dynamics, and by Peng et al. (2016), who investigated the wake of a five-blade cambered-airfoil turbine, respectively. Based on the results of full-scale field tests, Dabiri (2011) suggested that an array of closely-spaced and relatively small cross-flow wind turbines could extract up to an order of magnitude more power per land area than conventional AFT farms. He attributed the quick energy recovery observed to the significant vertical turbulent transport occurring in the CFTs' wakes. This point was also affirmed by Kinzel et al. (2012, 2015) who conducted more detailed measurements in a similar field test, but an erratum later pointed out that this turbulent transport contribution had been overestimated (Kinzel et al., 2013). Finally, Bachant & Wosnik (2015) used the acoustic Doppler velocimetry (ADV) technique to make detailed measurements on a plane normal to the freestream flow located at one turbine diameter downstream of the turbine's axis of rotation. They showed that the mean spanwise velocity field actually contributes more to the wake recovery than the turbulent transport in the case of a CFT wake. However, they performed their analysis on a single plane, thus preventing them to evaluate the contributions of the streamwise pressure gradient and the streamwise derivatives of the Reynolds and viscous stresses.

The present work aims to shed more light on the flow dynamics in the wakes of both the axial-flow turbine and the cross-flow turbine by conducting a quantitative analysis of all the different physical mechanisms affecting the wake's recovery. This is done by using the streamwise component of the time-averaged Unsteady Reynolds-averaged Navier-Stokes (URANS) equations and by comparing the contribution of each term appearing in this equation. Such a budget provides a direct evaluation of the rate at which the mean streamwise velocity is recovered in the turbines' wakes, unlike the more popular method based on the mean kinetic energy transport equation (Abkar & Porté-Agel, 2014; Cal et al., 2010; Hamilton et al., 2012; Lebron et al., 2012; Newman et al., 2014; VerHulst & Meneveau, 2014). The results of this study are therefore of great interest in an engineering point of view because the mean streamwise velocity is directly related to the energy available for a subsequent turbine in a turbine cluster. Moreover, solving the complete three-dimensional flow field allows us to evaluate all the terms affecting the wake recovery, which is usually not done experimentally due to the fact that some measurements are especially difficult to make without affecting the flow, such as is the case for the pressure field for example. Furthermore, many previous wake studies were restricted to the very near wake either because of the restrictions related to the available laboratory facilities or to the high computational costs in the case of numerical studies. In the current work, the wakes of the two turbine technologies are analyzed up to 12 diameters downstream of their center. Finally, our knowledge based on the axial-flow turbine's literature should be used carefully when studying cross-flow turbines because the conclusions drawn from the study of the former do not necessarily directly apply to the latter. Studies that compare the wakes of these two turbine concepts are very useful in that regard.

Information about the turbines' operating conditions, the turbines' geometry, the turbulence modeling approach and the numerical methodology are given in Sec. 2. The wake dynamics of the two turbine technologies are then analyzed in Sec. 3, the importance of all the mechanisms involved in the wake's recovery is evaluated in Sec. 4 and a discussion on the findings stemming from this work is presented in Sec. 5. The results of the present study provide novel and very valuable quantitative information about the detailed three-dimensional flow field in the wake of the AFT and the CFT concepts operating at a high Reynolds number.

2. Methodology

2.1. Description of the turbine cases investigated

The axial-flow turbine (Burton, 2011; Sørensen, 2011) is characterized by blades rotating at a constant velocity around an axis aligned with the direction of the oncoming flow while the cross-flow turbine concept (Paraschivoiu, 2002), also known as the vertical-axis turbine or the Darrieus turbine, involves blades that are rotating around an axis which is perpendicular to the flow. Outlines of both concepts are shown in Fig. 1.

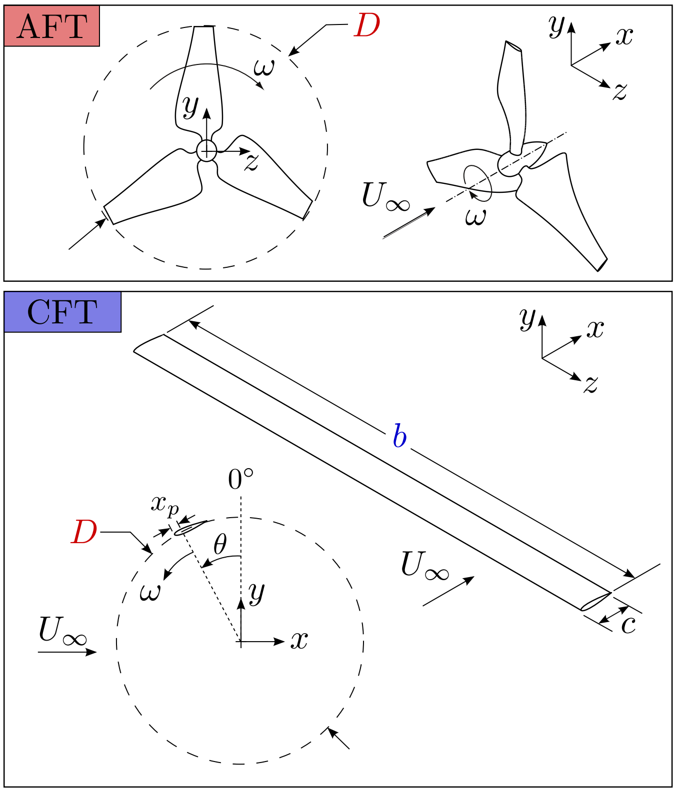

Figure 1: Outlines of the axial-flow turbine (top figure) and the cross-flow turbine (bottom figure) with the definition of the main geometric parameters.

The instantaneous power coefficient of these two turbine concepts is defined as:

$$C_p(\theta) = \frac{P(\theta)}{\frac{1}{2}\rho\, U_\infty^3\, A} \,, \tag{1}$$

where ρ is the density of the fluid, U_∞ is the freestream velocity and $P(\theta)$ is the instantaneous power extracted from the flow:

$$P(\theta) = M(\theta)\,\omega \,, \tag{2}$$

with $M(\theta)$ corresponding to the moment around the turbine's axis of rotation resulting from the force acting on the blade at a specific angle θ and ω being the turbine's angular velocity. Finally, A corresponds to the area swept by the blades, or in other words to the turbine's energy extraction plane, which corresponds to:

$$A = \begin{cases} \pi\, D^2/4, & \text{in the case of the AFT} \\ b\, D, & \text{in the case of the CFT} \end{cases} \,, \tag{3}$$

where D is the turbine's diameter and b is the blade's span length (see Fig. 1). The efficiency is then simply given by the cycle-averaged value of the power coefficient:

$$\eta = \frac{1}{2\pi} \int_0^{2\pi} C_p(\theta)\, d\theta \,. \tag{4}$$

Another important metric characterizing the turbines' performances is the mean drag coefficient of the turbine, defined as:

$$\overline{C_x} = \frac{1}{2\pi} \int_0^{2\pi} \frac{F_x(\theta)}{\frac{1}{2}\rho\, U_\infty^2\, A}\, d\theta \,. \tag{5}$$

where $F_x(\theta)$ is the instantaneous force component aligned with the oncoming flow.

The performances achieved by a turbine depend on its operating conditions, which include the tip speed ratio (λ):

$$\lambda = \frac{\omega\, D}{2\, U_\infty} \,, \tag{6}$$

and the Reynolds number, here based on the freestream velocity and the turbine's diameter:

$$\mathrm{Re}_D = \frac{U_\infty\, D}{\nu} \,. \tag{7}$$

Some other parameters characterizing the operation of the turbines such as the confinement as well as the turbulence level and the presence of perturbations in the oncoming flow may also affect the turbines' performances (Chamorro & Porté-Agel, 2009; Chu & Chiang, 2014; Kinsey & Dumas, 2016; Mycek et al., 2014a,b; Zhang et al., 2012). However, in this study, the turbines have been placed in an unconfined environment with a steady and uniform inflow in order to minimize the number of parameters influencing the problem. This allows for a more fundamental comparison between the two technologies by focusing on the intrinsic dynamics of the turbines' wakes in "ideal" conditions.

The tip speed ratio of each turbine concept has been chosen so that the turbines operate near their respective optimal efficiency conditions. The axial-flow turbine operates at a tip speed ratio of 3.5 and its geometry, based on a thicker version of the

SD8020 profile, has been developed by the University of Victoria (Klaptocz et al., 2014) to conduct a study on blockage and free surface effects in the context of the TC114 Marine Energy Standard (Marine Renewables Canada, 2014).

Regarding the cross-flow turbine, several different shapes have been proposed in the literature so far (Aslam Bhutta et al., 2012; Paraschivoiu, 2002), but this study only focuses on the H-Darrieus concept characterized by the use of simple straight blades that would be connected to the rotating shaft by some mechanical links. The CFT investigated in the current study corresponds to one of the single-blade turbines studied by Gosselin et al. (2016), which is characterized by a NACA0015 profile, a turbine's aspect ratio (b/D) of 15/7 and a diameter to chord length ratio of 7. It operates at a tip speed ratio of 4.25 which is slightly greater than the peak efficiency operating point and therefore stall is avoided (Gosselin et al., 2016). In the case of cross-flow turbines, some of the geometric parameters are often combined to form a dimensionless parameter called the solidity (σ), which is defined as:

$$\sigma = \frac{2\,N\,c}{D}\,, \tag{8}$$

where N is the number of blades and c is the chord length. The solidity value of the CFT studied in this work is around 0.286. The last relevant geometric parameter is the distance between the leading edge of the blade and the attach point that would link the blades to the rotor shaft (x_p). It is equal to a third of the chord length for the CFT considered. It is worth mentioning that the choice of a single-blade turbine instead of a more usual three-blade turbine has been made here in order to reduce the computational costs, as was done by Gosselin et al. (2016) in their study. Nevertheless, the present results are expected to be representative of any multiple-blade cross-flow turbines having the same efficiency, and thus the same solidity, tip speed ratio and blade's aspect ratio (b/c), as will be discussed in Sec. 5. The dynamic and geometric parameters characterizing both turbine concepts as well as their performances are listed in Table 1.

For comparison purposes, both simulations have been run at $\mathrm{Re}_D = 10^7$. This value roughly corresponds to a middle-size turbine. However, at such a high Reynolds number, the results presented in this study are expected to be essentially independent of an increase in the Reynolds number (Bachant & Wosnik, 2016; Chamorro et al., 2012a). The conclusions drawn from the current work should therefore also apply to large-scale turbines. Lastly, note that no turbine tower has been considered in the AFT simulation while no arms and no rotating shaft have been considered in the CFT simulation. Nonetheless, the simulations are expected to provide a faithful representation of complete turbines' wakes since the energy extraction process is mainly governed by the presence of the moving blades (Kang et al., 2012).

2.2. Turbulence modeling

It is important to note that an advanced turbulence modeling approach is needed to study the wake dynamics of turbines because the turbulent mixing occurring in their wakes is not adequately reproduced with a simple RANS/URANS approach relying on the Boussinesq hypothesis (Rethore, 2009). Also, representing the turbine through the use of body forces (Sanderse et al., 2011; Sørensen, 2011), with an actuator disk or an actuator line approach, leads to an approximation of the flow field in the near wake since the detailed flow field in the boundary layers next to the blades' surfaces is not solved. These approaches rather rely on tabulated aerodynamic data in order to determine the body forces based on the local flow conditions, which make them very sensitive to the aerodynamic data (Shamsoddin & Porté-Agel, 2014; Vermeer et al., 2003). Moreover, when the oncoming flow is unsteady in the blades' reference frame, such as is the case for the CFT concept, a dynamic stall model often has to be used along with the static airfoil data (Shamsoddin & Porté-Agel, 2014; Sørensen, 2011), hence adding to the uncertainty. In addition to the body forces, a source term might be needed to account for the turbulence generated by the blades when using an actuator disk approach (Sanderse et al., 2011). However, one would wish to make as few assumptions as possible that could affect the flow in the turbines' wakes in order to study the physics at play. This is especially true in the context of the current study where different turbine types are considered because different assumptions would have to be made depending on the geometric parameters and the operating conditions specific to each turbine type investigated. In other words, the results could undesirably become very dependent on the different assumptions made.

Based on the above discussion, simulations including the exact turbine blades' geometry have been carried out instead of using an actuator disk/line approach. Due to the fact that the RANS approach is not appropriate when one seeks to accurately capture the time-varying flow field and the intricate vortex dynamics in the wakes of turbines and because of the prohibitive computational cost of the LES approach, a hybrid methodology combining the RANS and the LES approaches, namely the Delayed Detached-Eddy simulation (DDES) ap-

Table 1: List of the dynamic and geometric parameters characterizing both turbine concepts as well as their performances. Note that the mean chord length has been used for the normalization in the case of the axial-flow turbine.

		AFT	CFT
Dynamic parameters	Re_D	10^7	10^7
	λ	3.5	4.25
Geometric parameters	Profile	Modified SD8020	NACA0015
	D/c	≈ 6	7
	x_p/c	-	1/3
	N	3	1
	b/D	-	15/7
Performances	η	40%	33%
	$\overline{C_x}$	0.74	0.89

proach (Spalart, 2009; Spalart et al., 2006), has been chosen in this work. This hybrid methodology uses a more cost efficient RANS approach in the attached regions of the flow near the walls, because of the less restrictive grid spacing requirements, and a more complete LES approach in the separated regions of the flow away from the walls.

The DDES approach is an improved version of the original Detached-Eddy Simulation (DES) approach (Shur et al., 1999; Spalart et al., 1997). It is based on the Spalart-Allmaras turbulence model which solves one transport equation for a modified turbulent viscosity ($\tilde{\nu}$) related to the eddy viscosity (ν_t) through an empirical relation (Spalart & Allmaras, 1994). Under the condition of local equilibrium, i.e., when the production term is balanced by the destruction term, this transport equation simplifies to the following simple relation (Spalart et al., 1997):

$$\tilde{\nu} \sim d^2 \tilde{S}_\nu \; , \tag{9}$$

where d is the distance between a point in the domain and the nearest solid surface and $\tilde{S}_\nu$ is the deformation parameter. This relation becomes analogous to a subgrid scale model used in LES simulations if d is replaced with a length scale (Δ) related to the local grid size, defined according to the following relation:

$$\Delta = \max(\Delta x, \Delta y, \Delta z) \; . \tag{10}$$

Therefore, in order to switch from a RANS to a LES formulation, the distance between a point in the domain and the nearest solid surface (d) is replaced with the parameter $\tilde{d}$:

$$\tilde{d} = \min(d, C_{DES} \cdot \Delta) \; , \tag{11}$$

where C_{DES} is a constant equal to 0.65 (Shur et al., 1999) and Δ is defined according to Eqn. 10. Following this procedure, a DES simulation remains in RANS mode as long as the distance between a point in the domain and the nearest solid surface (d) is smaller than the DES length scale (Δ) times the C_{DES} constant.

The Delayed Detached-Eddy Simulation (DDES) is a modified version of DES that has been created to overcome the possible issue of "grid induced separation" that could arise with some particular grid geometries (Spalart, 2009; Spalart et al., 2006). The purpose of this new version is to ensure that the turbulence modeling remains in RANS mode throughout the boundary layers. To do so, the definition of the parameter $\tilde{d}$ is modified as follows:

$$\tilde{d} = d - f_d \max(0, d - C_{DES} \cdot \Delta) \; , \tag{12}$$

where f_d is a filter function designed to take a value of 0 in attached boundary layers (RANS region) and a value of 1 in zones where the flow is separated (LES region) (Spalart et al., 2006). As recommended by Spalart (2009), the DDES formulation should be the new standard version of DES and it has therefore been chosen to conduct this study. As a complete discussion on DES and DDES modeling is out of the scope of this paper, the reader is referred to previous works that consider this matter more extensively (Spalart, 2009; Spalart et al., 2006, 1997; Spalart, 2000). Lastly, it is worthwhile to mention that Muscari et al. (2013) used the DES approach to study the wake of a marine propeller and observed a good agreement with the experimental results of Felli et al. (2011) using this turbulence modeling approach, but the agreement was poor when using a RANS approach.

2.3. Numerics

The finite-volume Navier-Stokes solver included in the CD-Adapco™ STAR-CCM+® software has been used to carry out the simulations (CD-Adapco™, 2014). Second-order schemes have been used for the temporal discretization, the diffusive flux as well as the convective flux. The scheme used for the convective flux is a hybrid bounded central-differencing scheme which combines upwind and centered schemes based on the procedure proposed by Travin et al. (2002) for DDES simulations. A segregated approach using the SIMPLE algorithm has been used for the pressure-velocity coupling.

The computational domain boundaries, shown in Fig. 2, are located far enough from the turbine so that the latter can be considered unconfined (Kinsey & Dumas, 2016), with a blockage ratio of:

$$\epsilon = A_{turbine}/A_{domain} < 0.004 \; . \tag{13}$$

A uniform and constant velocity as well as a turbulent viscosity ratio of $\nu_t/\nu = 3$ are set at the inlet boundary condition which is $15D$ upstream of the turbines. This turbulent viscosity ratio corresponds to a modified turbulent viscosity ratio ($\tilde{\nu}/\nu$) of 6.65 which follows the recommendation of Spalart and Rumsey (Spalart & Rumsey, 2007) made to ensure that the turbulence model is in fully turbulent mode. At the outlet, $30D$ downstream of the turbines, an average static pressure of zero is imposed and symmetry boundary conditions have been used on the four remaining surfaces of the computational domain. Regarding the initial condition, uniform velocity, pressure and turbulent viscosity ratio fields having the inlet boundary condition values are used throughout the domain.

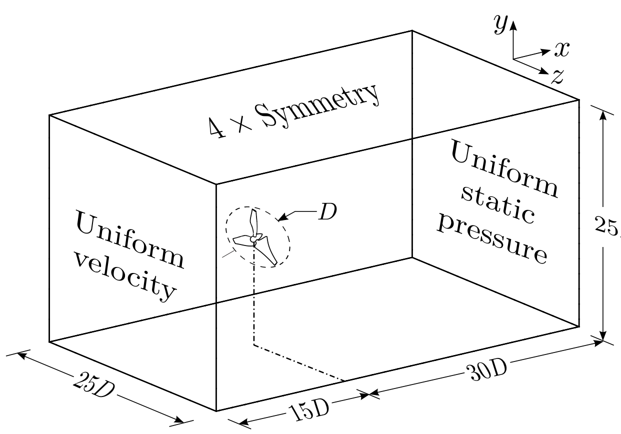

Figure 2: Computational domain and boundary conditions. Note that the turbine's center is located in the center of the domain in the y and z directions. Also, the axial-flow turbine shown is this figure is ten times bigger than the actual turbine for the sake of clarity.

A chimera grid technique has been chosen to deal with the blades' movement specific to each turbine concept. This approach, also known as the overset mesh technique, uses distinct grids for the background and the moving bodies, the two being superimposed. At each time step, an interpolation of the flow field is performed between the first overlapping cell layers of the background mesh and the moving mesh regions. The remaining overlapping cells of the background mesh region are temporarily inactive (CD-Adapco™, 2014).

The cell size is kept small in the whole wake region under investigation, which has been divided in four regions each consisting of several orthogonal cubic cells having a specified uniform size that differs from one region to the other. Note that the wake is analyzed only up to $12D$ downstream even if the refined mesh region extends up to $20D$ in order to prevent the results from being affected by the mesh coarsening starting at $20D$. The locations of the start and the end of the four refined regions of the background grid are given in Table 2 and the associated cell size (Δ_0) are given in Table 3.

Table 2: Locations of the start and the end of each of the four refined regions of the grid located in the wake normalized by the turbine's diameter $[x/D]$. Note that the origin of the coordinate system is located at the turbine's center.

		Zone 1	Zone 2	Zone 3	Zone 4
AFT	-0.25	1	5	15	20
CFT	-0.64	0.64	10	15	20

Table 3: Size of the orthogonal cubic cells (Δ_0) in each of the four refined regions of the grid normalized by the mean chord length (c).

	Zone 1	Zone 2	Zone 3	Zone 4
Δ_0/c	0.03	0.06	0.12	0.24

Regarding the moving mesh region, a polyhedral mesh with prism layers near the turbine surfaces have been used in the case of the AFT concept while a two-dimensional mesh consisting of quad elements has been extruded in the spanwise direction in the case of the CFT concept, as shown in Fig. 3. For both cases, the near-wall resolution has been chosen in order to ensure that the maximum dimensionless normal wall distance (y^+) remains around unity throughout the turbine's cycle with a maximum growth factor of 1.2 in the normal direction. The resulting total numbers of cells used for each of the two turbine concepts as well as an approximation of the CPU resources used to conduct the simulations are given in Table 4.

The temporal resolution has been chosen so that each complete turbine's rotation is divided into 1000 time steps, so that the time step is roughly equal to 0.005 convective time units

Table 4: Total number of cells forming the mesh of each turbine concept as well as the typical CPU resources required.

Case	Number of cells	Nb of cores	Runtime/cycle
AFT	62 118 147	156	53 h
CFT	133 761 744	336	37 h

($\Delta t \approx 0.005\, c/U_\infty$). This ensures that the local Courant number remains below one in the whole flow field, even in the moving mesh region where the highest local Courant number values are observed. This is a necessary condition in order to obtain a good level of accuracy in regions of the flow resolved in LES mode in the context of DDES simulations, according to Spalart (2001) and to Mockett et al. (2010). Assuming that the velocity in the wake roughly corresponds to $U_\infty/2$, the local Courant number in the most refined region of the background grid is around 0.1 for both turbine technologies.

The spatial and the temporal resolutions chosen in the current study have already proven to be adequate in previous studies on turbines (Gosselin et al., 2016; Kinsey & Dumas, 2012a,b). Moreover, two more simulations have been carried out for each turbine concept to conduct a resolution independence study. One simulation has been performed using a mesh two times coarser than the base case and the same temporal resolution and another simulation has been performed with the mesh's base case and a temporal resolution 50% finer. For both turbine concepts, the differences observed between the three simulations were found to be small enough for the base case simulation to be considered independent of the spatial and the temporal discretizations used. For example, the mean streamwise velocity on the wake centerline between 1 diameter and 12 diameters downstream of the turbines' center has been measured with the different resolution levels. The maximum local relative difference and the relative difference averaged over the entire line between these two additional simulations and the base case are presented in Table 5. The differences are given as a fraction of the freestream velocity.

Table 5: Difference between the mean streamwise velocity on the wake centerline of the base case with that of a simulation using a mesh two times coarser and one using a time step 50% smaller.

Case		Max difference	Mean difference
AFT	Coarse mesh	-5.6%	1.9%
	Fine time step	-6.5%	2.5%
CFT	Coarse mesh	-8.1%	3.2%
	Fine time step	-3.2%	1.3%

Since uniform velocity, pressure and turbulent viscosity ratio fields have been used as the initial conditions, the simulations must run for some time before recording any signal for further

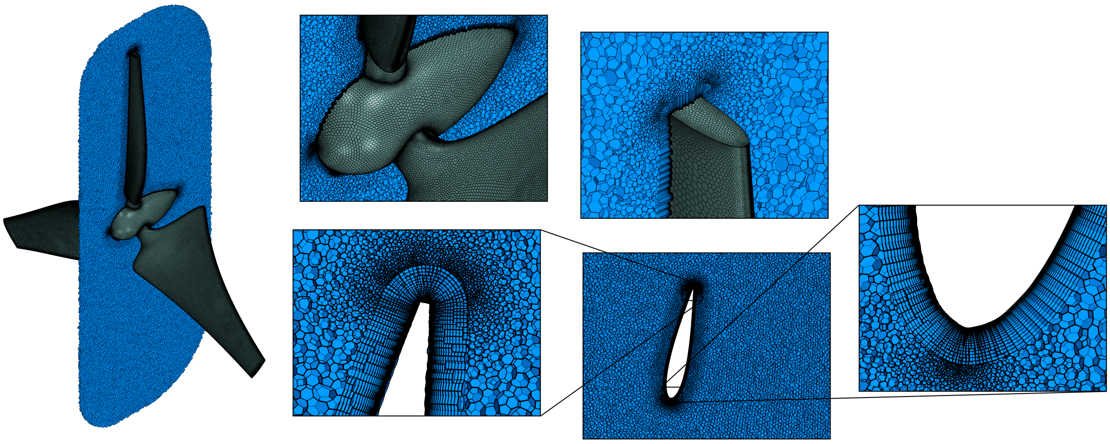

(a) The cells intersecting the $z/D = 0$ plane are shown in 3-D in the left figure and the two top figures while the cells intersecting the $y/D = 0.5$ plane are shown in the three other figures.

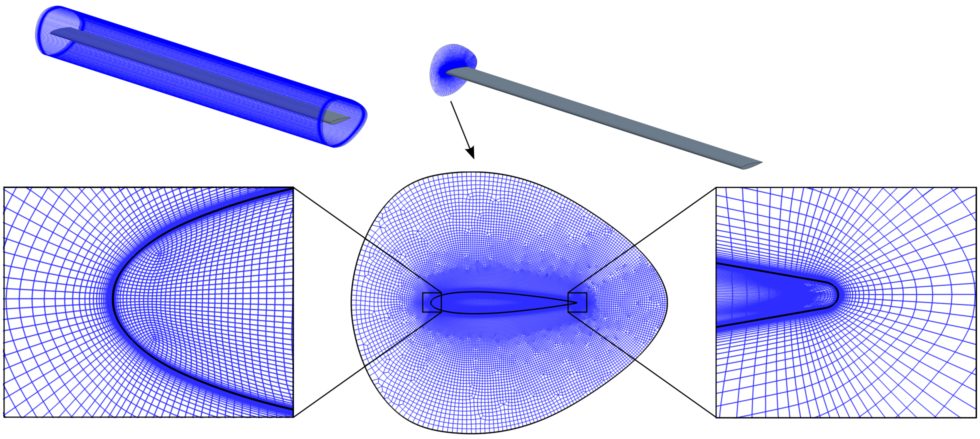

(b) Note that the moving mesh region extends past both ends of the blade in order to ensure that the overlapping cell regions, where interpolation between the background mesh and the moving mesh occurs, are not located near the blade tips.

Figure 3: Moving mesh region of the AFT case (top) and the CFT case (bottom).

statistical analysis in order to ensure that the initial flow field has convected far enough downstream to prevent the initialization from having an effect on the investigated wake region. If one assumes that the velocity in the wake roughly corresponds to $U_\infty/2$, the number of simulated cycles needed to convect the initial flow field over 12 turbine's diameters can be estimated. It has been chosen to let 6 more cycles elapsed than this estimation in order to account for the fact that the first few cycles are not representative of the cycle-to-cycle converged ones. The number of cycles elapsed before starting to record the flow field for the post-processing and the number of cycles during which the signals have been recorded to obtain a good statistical convergence are given in Table 6.

Table 6: Cycle at which the recording process has started (N_{start}) and number of cycles recorded ($N_{recorded}$) for statistical analysis.

	N_{start}	$N_{recorded}$
AFT	36	30
CFT	39	22

3. Wake dynamics

The wakes' topologies of the axial-flow turbine and the finite-aspect-ratio cross-flow turbine have been briefly presented in a preliminary study focusing on the vortex dynamics (Boudreau & Dumas, 2016). This section discusses the important aspects of the wakes with an emphasis on the transport mechanisms whose contributions are quantitatively evaluated in Sec. 4.

3.1. Axial-flow turbine

The axial-flow turbine studied in this work has an efficiency value of 40% under the current operating conditions. The vortex structures in its wake are shown in Fig. 4. As can be observed in this figure, the wake structure, which consists of tip vortices and root vortices, is rather well organized in the near wake. However, an instability is triggered around $1.5D$ for the root vortices and $2.5D$ for the tip vortices, which causes the whole vortex system to breakdown further downstream. This phenomenon is typical of axial-flow turbines' wakes and it has already been observed in several other studies (Chamorro et al., 2013b; Lignarolo et al., 2014; Mo et al., 2013; Sherry et al., 2013). By looking at Fig. 4b, it is found that the tip vortices travel faster downstream than the root vortices. As a result, the root vortices are closer to each other than the tip vortices in the near wake which make them more prone to undergo such an instability. This can partly explain why this instability occurs more upstream in the root vortices than in the tip vortices (Sherry et al., 2013). The same finding has also been reported by Zhang et al. (2012). Nonetheless, it is important to mention that these observations are strongly dependent on the turbine's geometric characteristics as well as its operating conditions, as will be discussed in more details in Sec. 5.

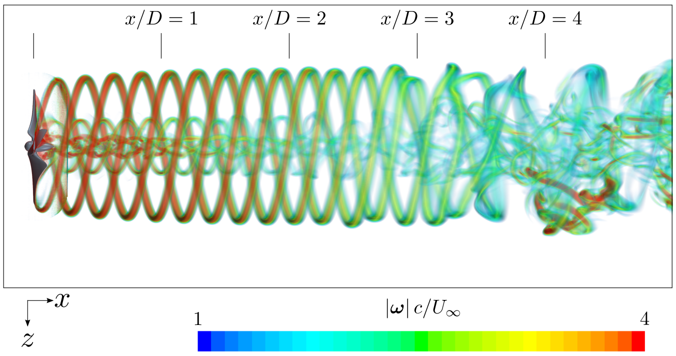

(a) Volume rendering of the vorticity magnitude in the wake of the axial-flow turbine. A video of the time evolution is available in the supplementary material.

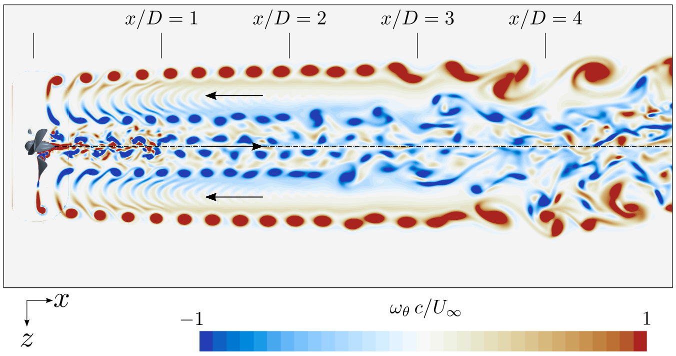

(b) Instantaneous tangential vorticity on the turbine's midplane ($y/D = 0$). The black arrows indicate the direction of the velocity induced by the tip and the root vortices.

Figure 4: Vortex dynamics in the wake of the axial-flow turbine.

Fig. 5a presents the mean streamwise, or axial, velocity contours in the wake of this turbine on a plane passing through the turbine's axis of rotation at $z/D = 0$. The near wake is found to be axisymmetric and characterized by a high velocity region in the wake center surrounded by an annular-shaped velocity deficit region, which has also been observed in several previous studies (Chatelain et al., 2013; Kang et al., 2012; Mo et al., 2013; Sherry et al., 2013; Tedds et al., 2014) using different turbine geometries. The annular-shaped velocity deficit observed in Fig. 5a is due to the presence of the strong root vortices in the near wake. As shown by the black arrows in Fig. 4b, the root vortices and the tip vortices induce alternating negative and positive mean streamwise velocity from the wake center to the edge of the wake. Further downstream, the mean streamwise velocity recovers and switches from an annular-shaped velocity deficit profile to a more usual Gaussian-shaped one.

Regarding the mean transverse, or radial, velocity component presented in Fig. 5b, one can first observe that its value is relatively small in a large fraction of the wake region. Additionally, it is found that, at both transverse edges of the wake, the direction of the mean transverse velocity switches from pointing away from the wake's centerline to pointing toward the wake's centerline at approximately $2.5D$ downstream of the turbine's center. In other words, the streamtube passing through the turbine's extraction plane expands over the first $2.5D$ in the wake and then starts to contract beyond this location. Note that this position corresponds to the position where the tip vortices become unstable.

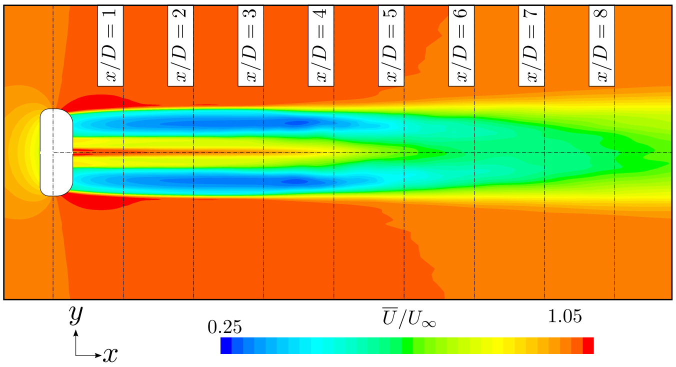

(a) Mean streamwise velocity on a plane passing through the turbine's axis of rotation ($z/D = 0$).

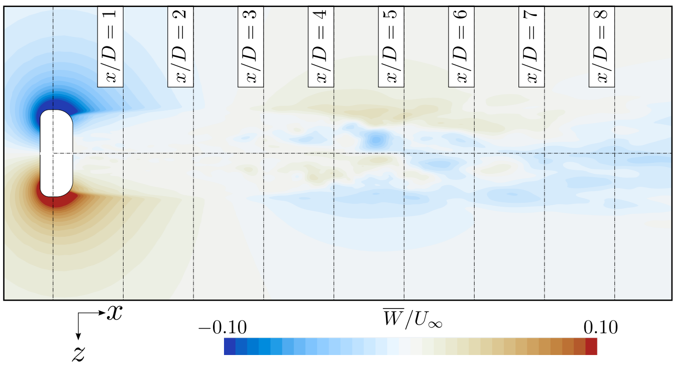

(b) Mean z velocity component on a plane passing through the turbine's axis of rotation ($y/D = 0$). Note that, on such a plane, this velocity component is equivalent to the mean radial velocity.

Figure 5: Mean velocity components in the wake of the axial-flow turbine. The white region corresponds to the area swept by the moving mesh region where the average flow field is not available.

Lastly, it is worthwhile to mention that the maximum mean streamwise velocity deficit is not observed very close to the turbine's center but rather further downstream at approximately $3.5D$ downstream. This decrease of the mean streamwise velocity in the near wake is mainly due to the presence of a mean adverse pressure gradient in this region of the flow field. This will be proved quantitatively in Sec. 4.

3.2. Cross-flow turbine

3.2.1. Infinite aspect ratio (2-D)

Unlike axial-flow turbines, cross-flow turbines are not axisymmetric and their wakes can be affected by different mechanisms occurring in the spanwise (z) and the transverse (y) directions. In order to gain a better understanding of the importance of the three-dimensional effects, a two-dimensional simulation (infinite turbine's aspect ratio) of the CFT case considered in this study is presented first for comparison purposes. This simulation has been carried out using the same temporal and spatial resolutions than the three-dimensional case, but the strain/vorticity-based formulation of the Spalart-Allmaras URANS turbulence model (Dacles-Mariani et al., 1995, 1999; Spalart & Allmaras, 1994) has been used instead of the DDES approach because the latter is restricted to three-dimensional simulations. Therefore, care must be taken when analyzing the results of this two-dimensional simulation since the turbulence modeling has a larger impact on the results with the URANS approach than with the DDES approach. Nevertheless, our main interest here is only to have a qualitative idea of the two-dimensional wake dynamics. Furthermore, the same conclusions as those described below have been drawn from another 2-D simulation using a different turbulence model, namely the $k-\omega$ SST model (Menter, 1994). Note also that this two-dimensional simulation ran over a sufficiently long time period for the initialization to convect over more than $20D$ before starting to average the flow fields over 67 cycles. It is worth mentioning that many of the 2-D CFT wake's aspects discussed in this section also apply to the 3-D CFT's wake.

The instantaneous power coefficient of the 2-D CFT is plotted in Fig. 6 along with the instantaneous power coefficient of the 3-D CFT. It is found that the evolution of C_p for the 2-D CFT is very similar to that of the 3-D CFT except than the values are smaller in the 3-D case because of the tip losses. For both cases, the peak power coefficient occurs around 100° and a negative power coefficient is observed during the whole downstream half of the cycle (180° – 360°) and even during the first 30 degrees. This means that the blade actually adds energy to the flow in this fraction of the cycle. Nevertheless, the efficiency value (η) is still positive and is equal to 46% for the 2-D CFT and to 33% for the 3-D CFT.

Contours of the instantaneous spanwise vorticity in the wake of the 2-D CFT are shown in Fig. 7. This figure highlights the presence of large vortex structures, the spanwise vortices, at both edges of the near wake. From Kelvin's circulation theorem, a variation in the blade's bound circulation must be accompanied by the shedding of an equal amount of circulation of opposite sign. In the upstream half of the blade's revolution, the blade's bound circulation increases from $\theta = 0°$

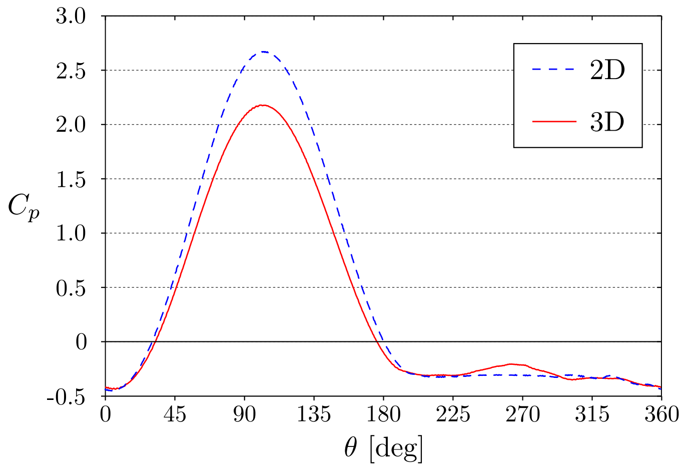

Figure 6: Instantaneous power coefficient for the 2-D CFT (dashed blue) and the 3-D CFT (solid red).

to around $\theta = 90°$, where the highest angles of attack are reached (Paraschivoiu, 2002), and then decreases in the remaining fraction of the upstream half of the turbine's cycle. As a result, net negative vorticity is shed from the upcoming blade region ($y/D > 0$) and net positive vorticity is shed from the retreating blade region ($y/D < 0$). The net positive or negative circulation of the shear layers shed by the blade is responsible for the roll-up of these shear layers in large vortex structures.

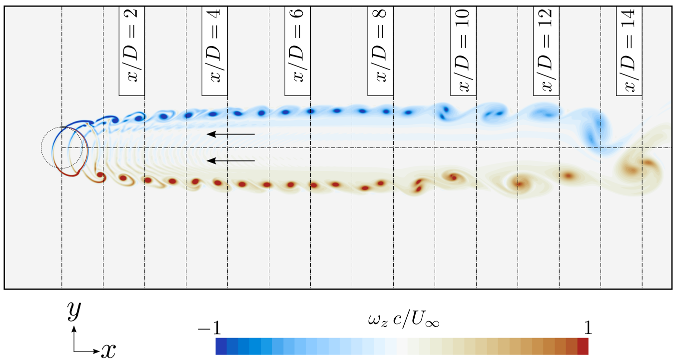

Figure 7: Instantaneous spanwise vorticity in the wake of the 2-D CFT. The black arrows indicate the direction of the velocity induced by the spanwise vortices.

In addition to these large spanwise vortices, shear layers are also observed in the central region of the very near wake. These shear layers correspond to the wake of the blade generated when the latter is located around 90° and in all the downstream half of the cycle. At these instants, the derivative of the blade's bound circulation with respect to time is expected to tend toward zero based on the instantaneous power coefficient evolution (see Fig. 6). Indeed, it is found that the instantaneous power coefficient is almost constant over all the downstream half of the cycle. Moreover, it is expected that the local angle of attack is much smaller there than in the upstream half of the cycle due to the fact that the streamwise velocity is smaller in the downstream half and also because the transverse velocity component pointing away from the wake center (positive y velocity in the $y/D > 0$ region and negative y velocity in the $y/D < 0$ region) increases. This results in an almost constant and small lift value in the whole downstream half of the cycle, and thus to an almost constant and small blade's bound circulation value in this fraction of the cycle, as was observed by Simão Ferreira et al. (2010). Since the derivative of the blade's bound circulation with respect to time tends to zero around 90° and in the downstream half of the cycle, the vorticity layers shed by the blade at these instants have zero net circulation. Consequently, these layers do not have the tendency to roll up and to form vortex structures, unlike those observed at both edges of the wake.

Another interesting feature of the 2-D CFT's wake is that an instability, similar to the one observed in the AFT's wake, occurs around $7.5D$ downstream of the turbine's center in the bottom half of the wake ($y/D < 0$) and around $8.5D$ in the upper half of the wake ($y/D > 0$), leading to a sudden transition in the wake topology. This phenomenon occurs closer to the turbine in the bottom half of the wake because the spanwise vortices are found to be stronger in this region of the wake compared to the upper half, as was also observed by Dixon et al. (2008).

As can be seen in Fig. 8a, showing the mean streamwise velocity contours in the 2-D CFT's wake, the maximum mean velocity deficit is observed relatively far downstream at approximately $11.5D$ downstream of the turbine's center. As is the case for the axial-flow turbine, this behavior is mainly attributed to the presence of an adverse pressure gradient in the near wake. The topology of the mean transverse velocity is also similar to that of the AFT because it is directed toward the edges of the wake in the near wake (for the first $7D$ in this case) before pointing toward the wake center further downstream. Again, it is found that the change in direction of the mean transverse velocity and the onset of the vortex instabilities (see Fig. 7) seem to be correlated as they both occur around the same location in the wake of the 2-D CFT, as is the case in the wake of the AFT.

It is also found that the 2-D CFT's wake is slightly asymmetric, unlike the axial-flow turbine's wake, with the maximum mean velocity deficit shifted toward the retreating blade region ($y/D < 0$). However, it is important to mention that this observation is highly dependent on the turbine's operating conditions. For example, a turbine for which stall occurs, typically in the retreating blade region of the upstream half of the cycle, can have a maximum velocity deficit shifted toward the upcoming blade region ($y/D > 0$) because much less energy is then extracted in the retreating blade region where stall occurs than in the upcoming blade region. The asymmetry observed in the specific case investigated in this work is related to the streamwise velocity induced by the large coherent vortices, or spanwise vortices, which are stronger in the retreating blade region ($y/D < 0$). Note however that the streamwise component of the force acting on the blade is almost symmetric between the upcoming and retreating blade regions.

3.2.2. *Finite aspect ratio (3-D)*

The 2-D CFT obviously corresponds to a limit case and it is interesting to compare its wake with that of a three-dimensional turbine having a finite aspect ratio. As will be discussed in the following, some important discrepancies are observed between the 2-D and the 3-D cross-flow turbines' wakes.

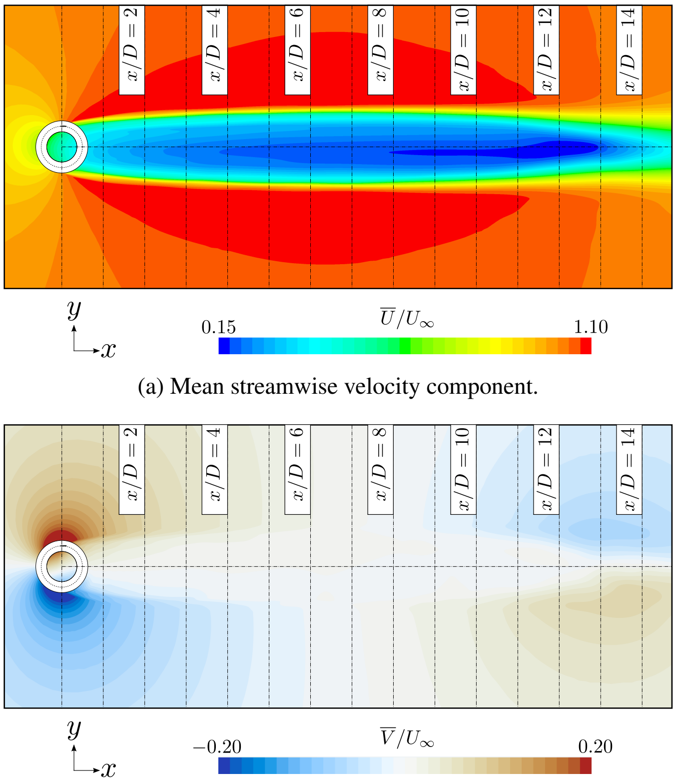

(a) Mean streamwise velocity component.

(b) Mean transverse velocity component.

Figure 8: Mean velocity components in the wake of the 2-D CFT. The white region corresponds to the area swept by the moving mesh region where the average flow field is not available.

The wake of the 3-D CFT differs from the 2-D case by the presence of tip vortices whose circulation varies during the blade's revolution. The circulation of the tip vortices is shown in Fig. 9. It has been measured at various instants of the turbine's cycle by computing the vorticity flux through appropriate plane sections encompassing the tip vortices. The dimensions of these plane sections have been determined by making sure that the circulation value is independent of a further increase of their size. Note that the circulation could not be computed in the downstream half because of the impossibility of differentiating the tip vortices shed in the downstream half from those shed in the upstream half that have convected downstream.

The strongest tip vortices are shed around $\theta \approx 90°$, i.e., the most upstream position of the blade, as was also observed by Simão Ferreira et al. (2010) and by Dixon et al. (2008). As mentioned in the previous section, this corresponds to the location of the highest angles of attack reached during the blade's revolution (Paraschivoiu, 2002). As for the 2-D CFT, the blade's bound circulation in the 3-D case is also expected to be much smaller and almost constant in the whole downstream half of the cycle. Therefore, the effects of the tip vortices generated in the upstream half around $\theta \approx 90°$ are dominant compared to the

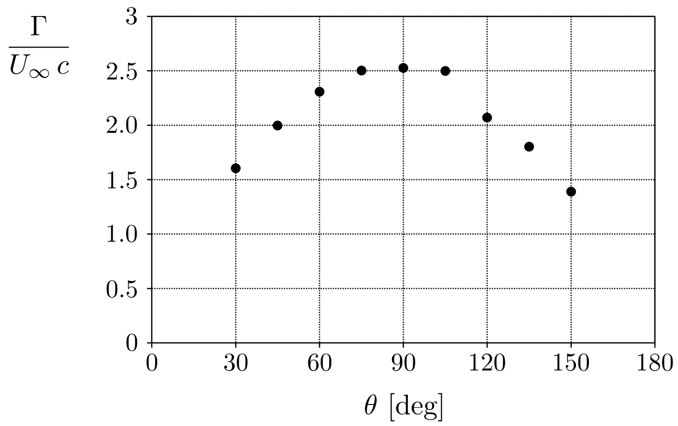

Figure 9: Circulation of the 3-D CFT blade's tip vortices at various instants during the upstream half of the turbine's cycle.

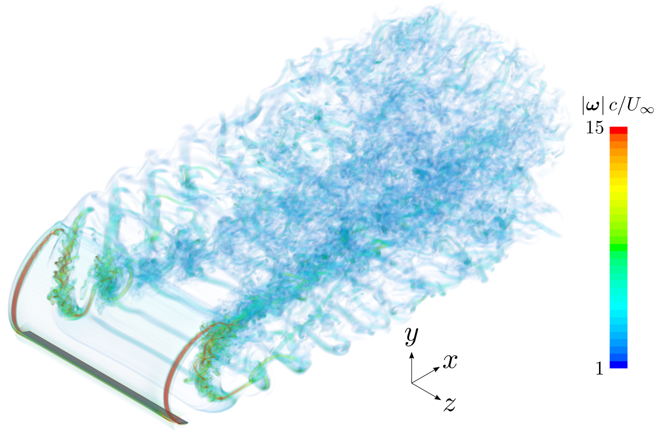

Figure 10: Volume rendering of the vorticity magnitude in the wake of the 3-D CFT shown up to $6D$ downstream of the turbine's axis of rotation. The blade is located at $\theta \approx 160°$. A video of the time evolution is available in the supplementary material.

effects of the tip vortices shed in the remaining of the turbine's cycle.

The complete three-dimensional wake's vortex dynamics is depicted in Fig. 10 by showing the vorticity magnitude through a volume rendering technique. The tip vortices are clearly seen as well as the spanwise vortex structures, similar to those found in the wake of the 2-D CFT, resulting from the variation in the blade's bound circulation during the blade's revolution. These spanwise vortices can be more clearly observed in Fig. 11a showing contours of the spanwise (z) vorticity component on the turbine's spanwise midplane ($z/b = 0$). One can easily notice that the topology of the spanwise vortices is significantly different than that of the 2-D CFT case (see Fig. 7) by the presence of a very irregular vorticity distribution in the wake's central region ($y/D \approx 0$). The velocity induction of the strong tip vortices generated around 90° is responsible for this phenomenon. Indeed, it causes the convection of the vorticity generated at both tips of the blade toward the spanwise midplane, as observed in Fig. 11b. It is found that the location where the vorticity is seen to reach the spanwise midplane in Fig. 11b corresponds to the onset of the irregular vorticity field observed in the central region of the spanwise midplane in Fig. 11a, namely around $2D$ downstream of the turbine's axis of rotation. Moreover, note that the large spanwise vortex structures eventually breakdown at approximately $3.5D$ because of the highly turbulent flow in the wake's central region and not because of the growth of an instability, as it was the case for the 2-D CFT and the AFT.

The tip vortices' spanwise velocity induction directed toward the midspan also explains the topology of the mean spanwise velocity field on the transverse midplane ($y/D = 0$) in the wake of the 3-D CFT, which is shown in Fig. 12a. Indeed, one observes that the mean spanwise velocity is always pointing toward the midspan. Additionally, its value is considerable and reaches up to 40% of the freestream velocity. The mean transverse velocity on the spanwise midplane ($z/D = 0$), presented in Fig. 12b, is also significant with a maximum value close to 25% of the freestream velocity. However, this velocity component is not directed toward the wake center but rather away from

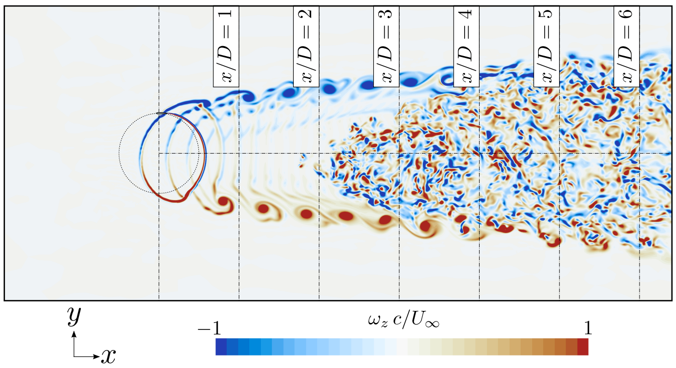

(a) Instantaneous spanwise vorticity on the spanwise midplane ($z/b = 0$).

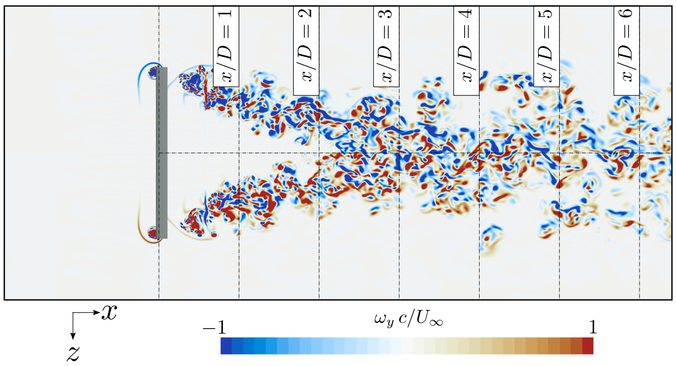

(b) Instantaneous transverse vorticity on the transverse midplane ($y/D = 0$).

Figure 11: Instantaneous vorticity in the wake of the 3-D CFT. In both figures, the blade is located at $\theta = 0°$.

it in the whole wake region investigated, unlike what has been observed in the cases of the 2-D CFT and the AFT. It is important to notice that the sudden increase in this transverse velocity pointing toward both edges of the wake observed around $2D$ coincide with the position where the high spanwise velocity reaches the midspan. All these observations can be summarized by saying that the strong tip vortices shed around 90° induce a net velocity oriented toward the midpsan resulting in the spanwise contraction of the wake, which in turn leads to the wake expansion in the transverse direction once the fluid coming from both tips of the blade reaches the midspan. It is therefore evident that the tip vortices and the spanwise velocity they induce play a crucial role in the wake dynamics of the 3-D CFT. It is also worthwhile to mention that the spanwise and transverse velocity components are much more important in the wake of the 3-D CFT than the same velocity components in the wake of the 2-D CFT or than the radial velocity component in the wake of the AFT.

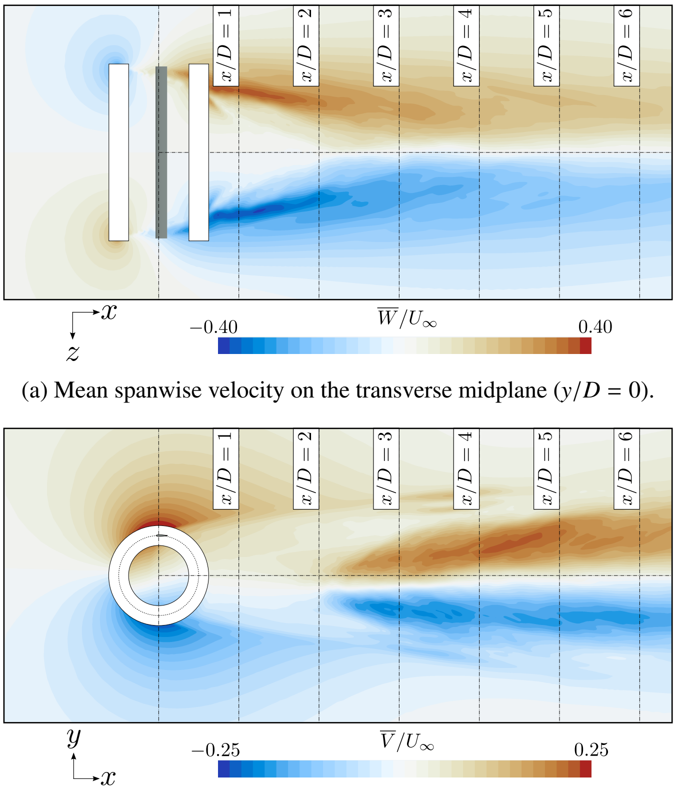

(a) Mean spanwise velocity on the transverse midplane ($y/D = 0$).

(b) Mean transverse velocity on the spanwise midplane ($z/b = 0$).

Figure 12: Mean velocity components in the wake of the 3-D CFT. The white region corresponds to the area swept by the moving mesh region where the average flow field is not available.

The previous observations only focused on the flow fields on the spanwise midplane ($z/D = 0$) and the transverse midplane ($y/D = 0$). In order to examine the remaining of the wake and to analyze in more details the shape of the velocity deficit region as one moves downstream, contours of the mean streamwise velocity on various planes perpendicular to the streamwise direction are presented in Fig. 13. The spanwise contraction of the wake on the transverse midplane and its expansion on the spanwise midplane discussed above are obviously also observed in this figure. However, one can notice that the spanwise contraction is only observed in the central region of the wake ($y/D \approx 0$), as the wake rather widens in the spanwise direction at both transverse edges of the wake (top and bottom of the black rectangles). One of the reasons is that the blade's bound circulation, and thus the tip vortices' circulation, is smaller when the blade is located at the two extreme transverse positions (see $\theta \approx 0°$ and $\theta \approx 180°$ in Fig. 9) than when it is around 90°. This results in a smaller spanwise velocity induction at both transverse edges of the wake than in the central region. Moreover, the fact that the paths of the tip vortices are curved has the same effect. Indeed, even if the tip vortices' circulation was constant over the whole upstream half of the turbine's cycle, hence forming a constant vortex having a shape similar to a semicircle, the higher velocity induction would still be observed in the central region as depicted in Fig. 14. Fig. 13 also reveals that this difference between the central region and the edges of the wake is not observed in the transverse direction where the wake is found to widen throughout the blade span length. Note that the contractions and the expansions of the wake found in the different regions of the flow field are in agreement with what has already been observed in the literature (Dixon et al., 2008; Simão Ferreira et al., 2010; Tescione et al., 2014).

Another interesting observation in Fig. 13 is that the wake of the 3-D CFT is asymmetric. Indeed, the velocity deficit is not only more pronounced but it is also wider in the spanwise direction for the upcoming blade region (top of the figures) than for the retreating blade region (bottom of the figures). Battisti et al. (2011), Bachant & Wosnik (2015) and Peng et al. (2016) also made similar observations on planes perpendicular to the oncoming flow in the very near wake of H-Darrieus turbines.

Lastly, contours of the mean streamwise velocity on the spanwise midplane ($z/b = 0$) are shown in Fig. 15. In the very near part of the wake ($x/D < 2$), the wake is slightly asymmetric with the maximum mean velocity deficit located in the retreating blade region ($y/D < 0$), as is the case for the 2-D CFT's wake (see Fig. 8a). However, the opposite behavior is observed further downstream with the maximum mean velocity deficit rather observed in the upcoming blade region, as was also observed in the experiments of Tescione et al. (2014) and Ryan et al. (2016). This is attributed to the fact that the spanwise contraction occuring in the wake's central region ($y/D \approx 0$) is slightly more pronounced in the retreating blade region than in upcoming blade region, as observed in Fig. 13. This spanwsie contraction is also responsible for the fact that the mean streamwise velocity is higher in the wake center than at both edges of the wake beyond approximately $2.25D$. This specific wake topology, which is strikingly different than those of the 2-D CFT and the far wake of the AFT, is far from being intuitive and the analysis of the whole wake dynamics has been needed to understand it. It is worth mentioning that this particular feature of the 3-D CFT's wake is seldom observed in the literature because most of the studies either only focus on the very near wake, thus missing this phenomenon (e.g., Bachant & Wosnik (2015); Tescione et al. (2014)), or consider a turbine with blades reaching both ends of a channel (e.g., Shamsoddin

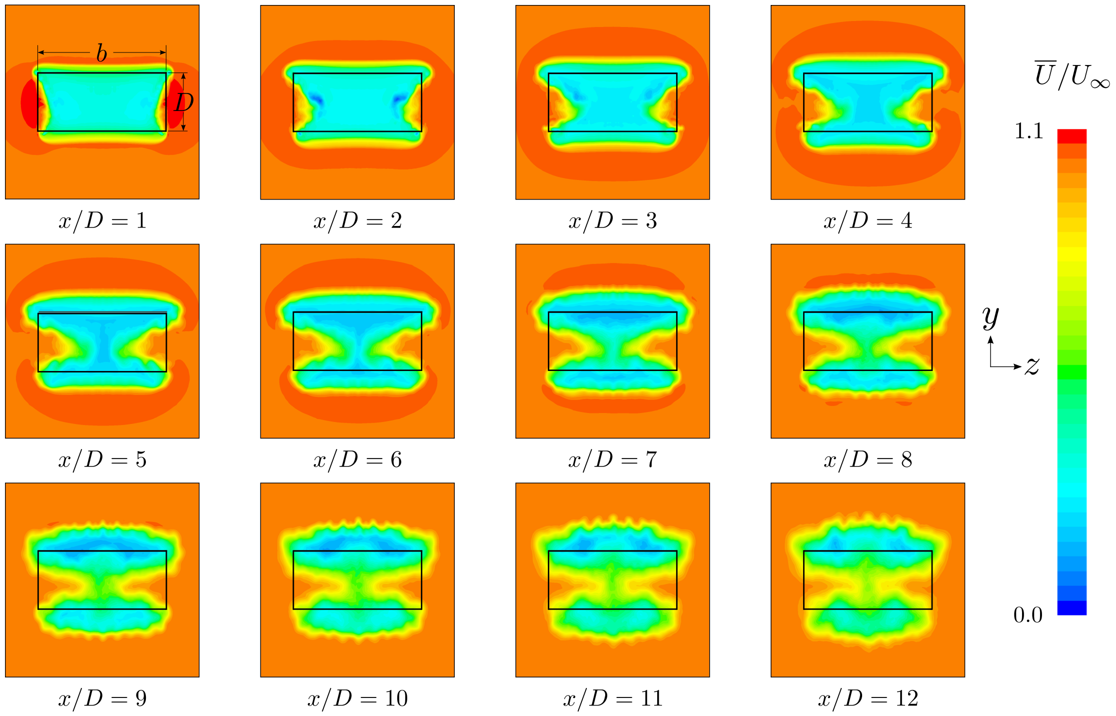

Figure 13: Mean streamwise velocity in the wake of the 3-D CFT on various planes perpendicular to the streamwise direction. Note that the black rectangles correspond to the shape of the turbine's extraction plane and that the upcoming blade region is located at the top of the rectangles while the retreating blade region is located at the bottom.

& Porté-Agel (2014)), hence affecting the tip effects which are responsible for this behavior.

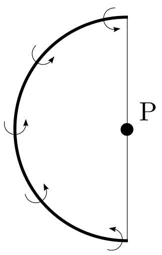

Figure 14: Schematics of the tip vortex generated in the upstream half of the turbine's cycle. The semicircle's center (point P) corresponds to the location where the highest velocity induction is observed on the line joining both ends of the vortex even when considering a hypothetical vortex having a constant circulation.

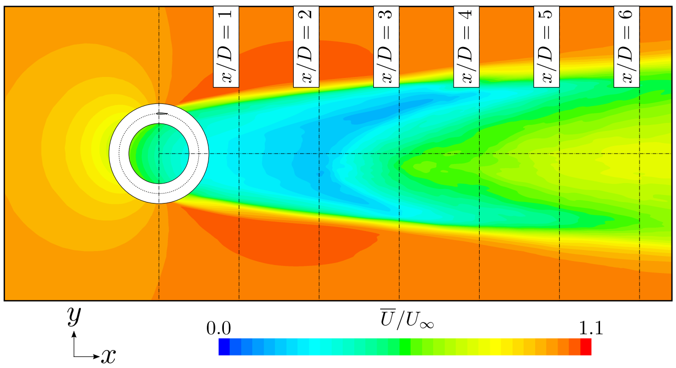

Figure 15: Mean streamwise velocity in the wake of the 3-D CFT on the spanwise midplane ($z/b = 0$). The white region corresponds to the area swept by the moving mesh region where the averaged flow field is not available.

4. Wake recovery rate budget

In order to evaluate the contributions of each transport process affecting the mean streamwise velocity recovery in the turbines wakes, the Unsteady Reynolds-averaged Navier-Stokes Equations (URANS) are used. When the Reynolds stresses are replaced by the term that models them in the context of the Spalart-Allmaras turbulence model (Spalart & Allmaras, 1994), which is the underlying turbulence model of the DDES approach used in this study, the URANS equations become:

$$\frac{\partial U_i}{\partial t} + U_j \frac{\partial U_i}{\partial x_j} = -\frac{1}{\rho}\frac{\partial P}{\partial x_i} + 2\frac{\partial(\nu S_{ij})}{\partial x_j} + 2\frac{\partial(\nu_t S_{ij})}{\partial x_j}, \quad (14)$$

where U is the velocity vector, P is the pressure, ν is the kinematic viscosity, ν_t is the turbulent kinematic viscosity, S is the strain rate tensor, t is time and x is the position vector. The last term on the right hand side of Eqn. 14 corresponds to the modeled turbulence.

All field quantities are then decomposed into a time-averaged component and a fluctuating component, respectively denoted by an overline and a prime symbol, and the whole equation is time-averaged. After some manipulations, the resulting equation in the streamwise direction, when normalized with U_∞/D, can be written as:

$$
\begin{aligned}
\frac{D}{U_\infty}\frac{\partial \overline{U}}{\partial x} = \frac{D}{U_\infty}\frac{1}{\overline{U}}\Bigg[& -\overline{V}\frac{\partial \overline{U}}{\partial y} - \overline{W}\frac{\partial \overline{U}}{\partial z} - \frac{1}{\rho}\frac{\partial \overline{P}}{\partial x} \\
& - \frac{\partial(\overline{U'U'})}{\partial x} - \frac{\partial(\overline{U'V'})}{\partial y} - \frac{\partial(\overline{U'W'})}{\partial z} \\
& + 2\frac{\partial(\overline{\nu_t}\,\overline{S_{1j}})}{\partial x_j} + 2\frac{\partial(\overline{\nu_t' S_{1j}'})}{\partial x_j} + \nu\frac{\partial^2 \overline{U}}{\partial x_j x_j}\Bigg] .
\end{aligned}
\tag{15}
$$

The term on the left hand side of Eqn. 15 corresponds to the streamwise component of the mean streamwise velocity gradient, which we shall refer to as the wake recovery rate. As for the terms on the right hand side of Eqn. 15, they correspond, from left to right, to the transport mechanisms by means of the transverse and the spanwise mean velocity fields, followed by the mean pressure gradient contribution, three transport terms involving correlations of fluctuating velocity components, two terms including ν_t, which are the transport terms associated to the modeled turbulence, and the viscous transport of the mean velocity field. The three terms with correlations of fluctuating velocity components represent the effects of the resolved unsteadiness of the flow field which we will refer to as the resolved fraction of turbulence, or the resolved Reynolds stresses. This rearrangement of the time-averaged URANS equation in the streamwise direction allows the relative importance of each transport mechanism contributing to the wake recovery rate to be assessed.

Before presenting the wake recovery rate budget, the evolution of the mean streamwise velocity and the mean streamwise energy flux in the wake of the two turbine concepts are first shown in Fig. 16. In order to get an idea of the power available for a hypothetical downstream turbine, the values have been spatially averaged over successive plane sections normal to the streamwise direction and having the same dimensions and the same shape as the turbines' extraction planes (angle brackets are used to denote a spatial-averaged variable). Note that because of the non-uniformity of the flow fields over the plane sections used for the spatial-averaging process, the section-averaged cubic values differ from the cube of the section-averaged mean streamwise velocity values. A similar procedure has been used by Bachant & Wosnik (2015) for the study of a cross-flow turbine's wake in a towing tank and by Mycek et al. (2014a) for an axial-flow turbine's wake. However, Mycek et al. (2014a) did not compute the various momentum transport terms while Bachant & Wosnik (2015) only computed them on a single plane and they therefore could not evaluate all the terms involving streamwise derivatives.

It is found that, while the section-averaged mean streamwise velocity is always increasing in the wake of the CFT, it decreases up to around $3D$ downstream of the AFT's center and then starts to increase further downstream. In other words, the wake recovery rate is negative in the near wake of the AFT. However, it is also observed that the wake recovery rate of the AFT becomes positive and is higher than that of the 3-D CFT beyond around $4D$ so that the values of the section-averaged mean streamwise velocity for the AFT tend to get closer to the values observed in the case of the 3-D CFT. At $12D$, there is a 16.6% difference in the available section-averaged power between the two technologies. Considering that the difference between their efficiency values is 7% (η = 40% for the AFT and η = 33% for the 3-D CFT), this suggests that the 3-D CFT makes a better use of the power passing through its extraction plane. However, this conclusion only applies to the specific turbines considered in this study and at this location in the wake. Further studies are needed if one hopes to carry out a general conclusion stating which technology is characterized by the quickest wake recovery. Actually, this might not even be possible as the operating and ambient conditions could affect which technology is showing the highest recovery. It is worth recalling here that the objective of this work is not to perform such a conclusion but rather to find what are the important mechanisms responsible for the wake recovery for both turbine concepts.

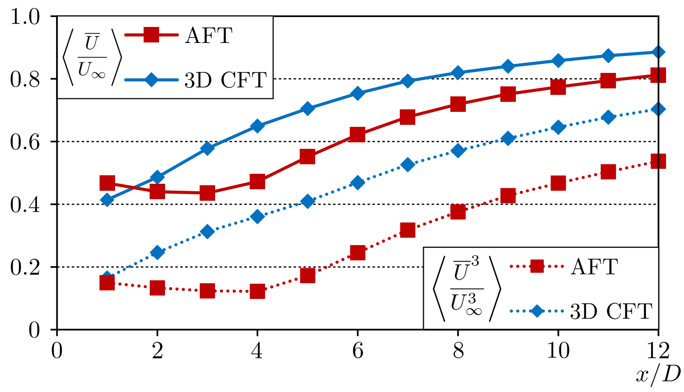

Figure 16: Section-averaged mean streamwise velocity and mean streamwise energy flux.

Evaluating all the terms appearing in the budget allows us to ascertain that it is balanced, or in other words, that the sum of all the terms on the right hand side of Eqn. 15 is equal to streamwise derivative of the mean streamwise velocity component appearing on the left hand side of this equation. The comparison between the values of left hand side and the right hand side of Eqn. 15 for both turbine concepts is shown in Fig. 17. As for the evolution of the mean streamwise velocity and its cubic value shown in Fig. 16, the value of each term in the budget has been computed and section-averaged at every turbine diameter from $1D$ to $12D$.

It is found in Fig. 17 that the left hand side and the right hand side (the sum of all terms) of Eqn. 15 match well both for the AFT and the CFT, which validates the methodology used to compute the value of every term in the budget. This figure confirms what was previously observed, namely that the wake recovery rate of the AFT is negative in the near wake, unlike the wake recovery rate of the CFT, but becomes higher than the recovery rate of the CFT beyond $4D$. Lastly, one can notice that the wake recovery rates of both technologies asymptoti-

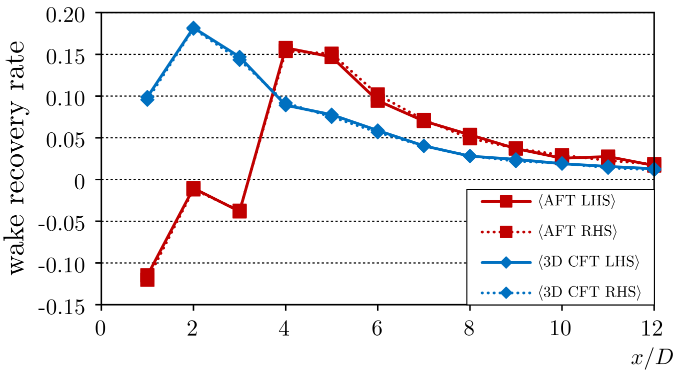

Figure 17: Comparison between the section-averaged value of the streamwise derivative of the mean streamwise velocity component (LHS) and the sum of all the terms appearing on the right hand side of Eqn. 15 (RHS) for the AFT (red) and the 3-D CFT (blue).

cally reach the same value at $12D$, hence suggesting that the difference in the available section-averaged power, observed in Fig. 16, should remain around 15% over a certain distance past $12D$.

The complete budget of the wake recovery rate (Eqn. 15) is plotted in Fig. 18 for the AFT and the 3-D CFT. An adverse pressure gradient ④ is observed in both turbines' near wake, which leads to a significant negative contribution to the wake recovery rate ① (see Fig. 18). In both cases, the freestream pressure value is essentially recovered beyond $6D$ downstream. Regarding the modeled fraction of the turbulent transport ⑧ and the viscous transport of the mean velocity field ⑨, they are both found to be negligible compared to the other contributions for the two turbine technologies considered and for the whole wake region under investigation. Note that the curve corresponding to the viscous transport of the mean velocity field ⑨ can hardly be seen in Fig. 18 because it is hidden by the curve corresponding to modeled fraction of the turbulent transport ⑧. The very small contribution from the viscous transport of the mean velocity field ⑨ was expected because of the high Reynolds number considered in the current work.

Despite these similarities, the evolution of the wake recovery rate in the wake of the AFT is notably different than the one characterizing the 3-D CFT. In the case of the AFT, the negative wake recovery rate ① observed for the first three diameters downstream of the turbine's center closely follows the evolution of the mean pressure gradient contribution because the other terms are either smaller or almost cancel out at $3D$. The maximum recovery rate is observed at $4D$, with a value of 15.8%. The main transport mechanism contributing to this peak value is the turbulent transport by means of the resolved transverse Reynolds stresses (⑥ and ⑦). Actually, it is observed that this contribution stays the dominant one for the remaining of the wake region investigated. The high values of this term around $4D$ are related to the onset of the pairing instability in the tip vortices occurring around $3D$ (see Fig. 4). Regarding the transport due to the mean transverse flow field (② and ③), it switches from a negative contribution to a positive contribution around $2D$ because of the change in direction of the mean transverse flow field (see Fig. 5b). In other words, its contribution becomes positive when the mean streamtube starts to contract after its expansion in the near wake. The fact that the contributions of the mean transverse flow field and the resolved transverse Reynolds stresses both reach a maximum value at the same location, just downstream of the location where an instability starts to grow in the tip vortex system, clearly demonstrates that all these phenomena are closely related to one another.

In the case of the 3-D CFT, the maximum recovery rate ① is observed at $2D$ downstream, which is closer to the turbine than in the case of the AFT's wake, and its value of 18.2% is also higher than the maximum wake recovery rate observed for the AFT. Furthermore, the dominant process affecting the wake recovery rate is also different. In the case of the 3-D CFT, it is the transport by means of the mean spanwise velocity field ③ that is the main transport mechanism, as was also observed by Bachant & Wosnik (2015). This contribution is associated to the spanwise contraction of the wake due to the velocity induced by the strong tip vortices generated around $\theta = 90°$. The high wake recovery rate reported in the literature for the CFT compared to the AFT (Dabiri, 2011; Kinzel et al., 2012) could therefore be partly attributed to the transport by the mean spanwise flow field, which is only significant in the case of the 3-D cross-flow turbine. As observed by Bachant & Wosnik (2015), the contribution of the mean transverse velocity field ② is negative at $1D$ downstream of the turbine's axis of rotation. The current study shows that this contribution remains negative at $2D$ but then becomes positive further downstream. This is due to the fact that, while the mean transverse velocity $(\overline{V})$ is positive in the upcoming blade region $(y/D > 0)$ and negative in the retreating blade region $(y/D < 0)$ in the whole wake region investigated (see Fig. 12b), the sign of the term $\partial\overline{U}/\partial y$ changes around $2.5D$ downstream of the turbine's axis of rotation. Indeed, by looking at Figs. 13 and 15, one can notice that the maximum velocity deficit is located around the wake's central region in the very near wake while it is located at the edges of the wake further downstream. Lastly, the turbulent transport terms are found to be of secondary importance compared to the transport terms associated to the mean flow field in the wake of the 3-D CFT, which is considerably different than what is observed in the case of the AFT's wake.

It is also worth mentioning that the budget of the wake recovery rate of the 2-D CFT (not shown) revealed a behavior similar to the one associated to the axial-flow turbine with a negative mean streamwise velocity recovery rate in the near wake followed by the presence of a sharp positive peak observed past the location where the vortex system breakdown is observed (see Fig. 7). This highlights the importance of the turbine's aspect ratio (infinite in this 2-D case) on the wake dynamics and it also suggests that two-dimensional models are only of limited value for the study of finite-aspect-ratio cross-flow turbines' wakes, at least for turbines having an aspect ratio similar to the one considered in this study $(b/d = 15/7)$.

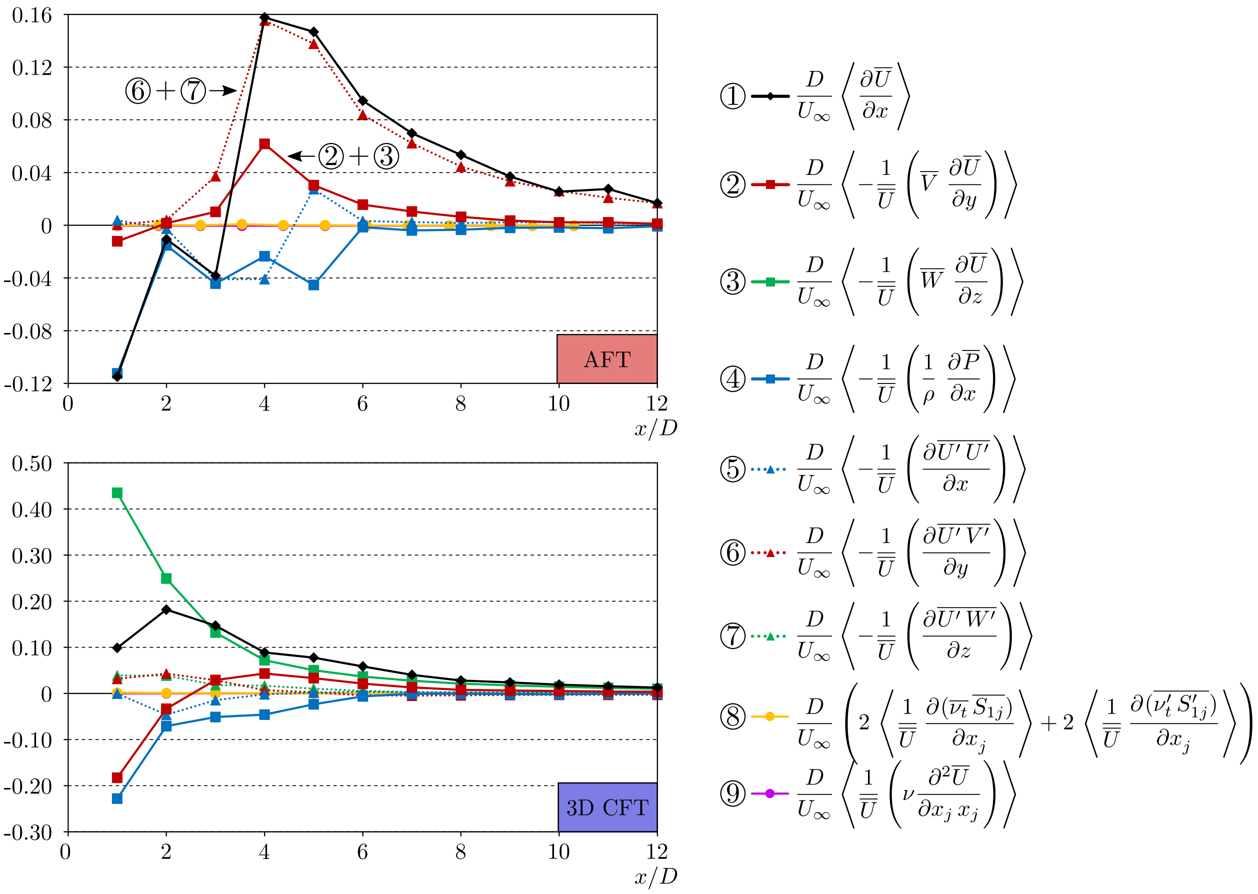

Figure 18: Budget of the wake recovery rate for both turbine cases (see Eqn. 15). Each term has been section-averaged over successive plane sections having the same shape and the same size as the turbines' extraction plane. Note that in the case of the AFT, the terms associated to the mean flow field and to the resolved part of the Reynolds stresses involving the two transverse directions have been combined in pairs due to the fact their values are the same because of the axisymmetry of this technology.

5. Discussion

Since the mean streamwise velocity recovery rate in the AFT's wake seems highly related to the development of an instability in its wake vortex system, the wake recovery rate is expected to be strongly sensitive to the characteristics of the upstream flow such as the turbulence intensity, as already pointed out in previous studies (Bastankhah & Porté-Agel, 2014; Chamorro & Porté-Agel, 2009; Chu & Chiang, 2014; Medici & Alfredsson, 2006; Mycek et al., 2014a; Sanderse et al., 2011; Zhang et al., 2012). Nevertheless, it is expected that the main mechanism affecting the wake recovery, namely the vortex system instability and breakdown, stays the dominant process even with a more turbulent oncoming flow. The location where this phenomenon occurs should however be affected (Chatelain et al., 2013; Felli et al., 2011; Zhang et al., 2012). Indeed, the higher the turbulence level, the sooner the instability would be triggered. This could explain why higher recovery rates have been observed in the wake of a turbine located in the wake of another one (Chatelain et al., 2013; Mycek et al., 2014b).

The wake dynamics of the AFT is also expected to be highly dependent on the tip speed ratio and the number of blades. A higher tip speed ratio for a given number of blades or a higher number of blades for a given tip speed ratio would result in a shorter distance between two successive tip vortices and the onset of the instability should therefore move upstream (Felli et al., 2011; Lignarolo et al., 2014; Sherry et al., 2013). Lastly, the blade geometry should also greatly affect the wake dynamics since a different geometry could result in a different loading distribution, which in turn would lead to a different tip vortex strength or to a different vorticity distribution in the tip vortices, both playing an important role in the onset of the instability (Felli et al., 2011; Sherry et al., 2013).

As mentioned earlier, the wake dynamics of the 3-D CFT is largely influenced by the strong tip vortices shed in the upstream half of the cycle. Consequently, every factor affecting these tip vortices and the velocity they induce are expected to have a significant impact on the CFT's wake topology. One of the most importants parameter is obviously the turbine's aspect ratio. The wake analysis of small-aspect-ratio CFTs and large-aspect-ratio CFTs will therefore be made separately in the following.

As for the AFT's wake, a different tip speed ratio or a different number of blades could also modify the small-aspect-ratio

CFT's wake topology, but not in the same way. Indeed, these two parameters cannot affect the location of the onset of an instability since no such phenomenon is observed in small-aspect-ratio CFTs' wakes such as the one analyzed in this work. However, they could alter the intensity of the tip vortices and thus could potentially affect the wake dynamics. Actually, anything affecting the tip vortices, such as the presence of end plates, could have an impact on the wake topology. Regarding the tip speed ratio, it is not straightforward to predict its influence on the blade's bound circulation. The theoretical angle of attack is known to decrease as the tip speed ratio increases, resulting in lower circulation values, while the velocity in the blade's reference frame is expected to increase, which has the opposite effect on the blade's bound circulation (Paraschivoiu, 2002). Nevertheless, the experimental measurements of Bachant & Wosnik (2013) conducted at $1D$ downstream of a CFT having a turbine's aspect ratio of 1 showed an increase in the spanwise velocity component directed toward the wake center as the tip speed ratio was increased from 0.1 to 3.1. Moreover, Ryan et al. (2016) experimentally observed that the recovery rate of the section-averaged mean streamwise velocity increases with the tip speed ratio.

As most of the commercial CFTs have three blades and not just one, one may wonder what is the effect of the number of blades on the wake dynamics. In order to compare two turbines with equivalent performances, the solidity, the tip speed ratio and the blade's aspect ratio (b/c) must be the same for both (Gosselin et al., 2016; Paraschivoiu, 2002). Considering two turbines having the same blade's chord length and placed in the same freestream velocity for example, the radius of a three-blade turbine would be three times larger than that of a single-blade turbine. Consequently, such a three-blade turbine would roughly extract three times more energy than the corresponding single-blade turbine but in an extraction plane which is three times larger. The loading on each blade of the three-blade turbine should therefore be approximately the same as the loading on the blade of the single-blade one, hence leading to tip vortices having a similar intensity. For the tip speed ratio to be the same, the angular velocity of the three-blade turbine has to be three times smaller than that of the single-blade turbine but the former shed three vortices per revolution compared to one for the latter. As a result, the distance between two successive tip vortices (see for example Fig. 10) would be identical for both turbines. We can therefore conclude from this that the general wake topology of a multiple-blade turbine should be similar to that of a single-blade turbine when the efficiency is the same for both (same solidity, tip speed ratio and blade's aspect ratio). Even if Gosselin et al. (2016) have shown that the efficiency is not precisely the same when the number of blades is modified, it remains close and therefore no significant differences are expected in the general wake dynamics. This is further confirmed by the fact that a similar wake dynamics with large mean spanwise velocities have also been reported in the literature for the wake of three-blade CFTs (e.g., Bachant & Wosnik (2015); Tescione et al. (2014)).

Small-aspect-ratio CFTs are expected to be much less dependent and sensitive to the turbulence level in the oncoming flow than AFTs because the mean flow field in their wake is predominantly affected by their geometric characteristics and their operating conditions. This is a particularly interesting feature specific to this unsteady turbine technology. First, it should greatly facilitate the prediction of turbine arrays' performances because the wake of every turbine should not be significantly affected by the turbulence generated by a turbine located upstream. Second, it suggests that the performances of small-aspect-ratio CFT arrays should be less sensitive to variations in the oncoming flow conditions. However, small-aspect-ratio CFTs are known to be less efficient individually than large-aspect-ratio CFTs because of the larger tip losses (Gosselin et al., 2016; Li & Calisal, 2010). Further studies are therefore needed in order to determine what would be the optimal choice in terms of the turbine's aspect ratio for a given turbine farm.

On the other hand, the higher the aspect ratio, the more the wake dynamics will resemble that of the 2-D case, which has proved to be similar to the AFT's wake in the sense that the onset of an instability seems to be the main mechanism affecting the wake recovery rate. Consequently, the parameters affecting the wake dynamics of the AFT should also apply to large-aspect-ratio CFTs in the same way. Li & Calisal (2010) have declared that such a two-dimensional behavior is observed for CFT having a turbine's aspect ratio greater than 3.5.

Finally, the results of the current study suggest that an aligned turbine farm layout could be optimal in the case of a small-aspect-ratio CFT array because most of the velocity deficit is quickly found away from the wake center (see Fig. 13). A staggered configuration could however be more efficient in the case of large-aspect-ratio CFT arrays, as is the case for AFT arrays (Chamorro et al., 2011).

6. Conclusion

Three-dimensional simulations of two different turbine concepts, the axial-flow turbine and the cross-flow turbine, have been conducted using the Delayed Detached-Eddy Simulation (DDES) turbulence modeling approach. The objective of this work was to compare the wake recovery rate of these turbine technologies and to develop a better understanding of the physics at play by assessing the relative importance of all the momentum transport processes.

The wake dynamics of the two turbine concepts have been analyzed with an emphasis on the vortex dynamics. The AFT's wake has revealed the presence of an instability in the tip and the root vortices leading to an enhanced turbulence mixing, which has been found to be mainly responsible for the wake recovery. Regarding the CFT, a clear distinction has been observed between the 2-D turbine's wake and the 3-D turbine's wake. While the dynamics of the former resembles that of the AFT's wake, with the triggering of a vortex instability as the dominant mechanism affecting the wake recovery, the dynamics of the latter is rather mostly affected by the strong velocity inductions by the tip vortices shed in the upstream half of the turbine's cycle, which results in a contraction of the wake's central region in the spanwise direction.

Each contribution affecting the wake recovery rate have been assessed and compared by using the time-averaged Unsteady Reynolds-averaged Navier-Stokes equation in the streamwise direction as a post-processing tool. The resulting budget has shown that the mean pressure field has a significant negative contribution in the very near wake, even if the turbines considered in this study are essentially unconfined. In the case of the AFT's wake, the wake recovery rate is negative in the near wake and becomes positive further downstream essentially due to the rise of the contributions from the resolved transverse Reynolds stresses following the vortex instability. The maximum wake recovery rate in the wake of the 3-D CFT is both higher and observed closer to the turbine than in the AFT's wake due to the dominant positive contribution from the mean spanwise flow field. The results of the current study suggest that the AFT's wake dynamics should be more sensitive to the turbulence level in the oncoming flow than the 3-D CFT's wake dynamics. The latter is expected to be mostly affected by the geometric characteristics, such as the turbine's aspect ratio, and the operating conditions.

The conclusions of this work have led to a better understanding of the physical processes at play in the turbines' wakes and could therefore be useful to develop simpler models which are more suited to carry out optimization studies of turbine farm layouts involving any of the two different turbine technologies considered.

Future studies devoted to the impact of different turbine geometries, operating conditions and specific site characteristics on the wake recovery rate budget are needed. This could include the use of non-uniform and time-varying inflow conditions and the presence of shear or misalignment in the oncoming flow, which can be more representative of real-site scenarios. The results presented in this study should serve as references to which "real-site" cases could be compared, thereby allowing to discriminate between the intrinsic wake dynamics of each technology and the "real-site effects". In this study, the two turbines have been compared at their respective optimal operating point. Comparing the wakes of turbines having the same mean drag coefficient could also provide some useful additional information. Furthermore, since carefully designed end plates are known to improve significantly the efficiency of a cross-flow turbine (Gosselin et al., 2016), the consequences of their use on its wake dynamics should also be investigated in future works.

Lastly, previous preliminary works (Boudreau & Dumas, 2016) have shown that the wake topology of the oscillating-foil turbine, an other type of cross-flow turbine, shares several similarities with the wake of the cross-flow turbine analyzed in the current study. It would be interesting to conduct for this technology the same quantitative analysis that has been presented in this paper in order to investigate its wake more deeply.

7. Acknowledgements

Financial support from the Natural Sciences and Engineering Research Council of Canada (NSERC) and the Fonds de recherche du Québec - Nature et technologies (FRQ-NT) is gratefully acknowledged by the authors. Computations in this work were run on the supercomputers Guillimin from McGill University and Colosse from Laval University, managed by Calcul Québec and Compute Canada. The authors would also like to thank their colleagues at the LMFN Sébastien Bourget for the revision of the wake recovery rate budget derivation and professor Mathieu Olivier for the revision of this manuscript.

References

Abkar, M., & Porté-Agel, F. (2014). Mean and turbulent kinetic energy budgets inside and above very large wind farms under conventionally-neutral condition. *Renewable Energy*, *70*, 142–152. doi:10.1016/j.renene.2014.03.050.

Aslam Bhutta, M. M., Hayat, N., Farooq, A. U., Ali, Z., Jamil, S. R., & Hussain, Z. (2012). Vertical axis wind turbine - A review of various configurations and design techniques. *Renewable and Sustainable Energy Reviews*, *16*, 1926 – 1939. doi:10.1016/j.rser.2011.12.004.

Bachant, P., & Wosnik, M. (2013). Performance and Near-Wake Measurements for a Vertical Axis Turbine at Moderate Reynolds Number. In *ASME 2013 Fluids Engineering Division Summer Meeting* (p. (9 pp.)). doi:110.1115/FEDSM2013-16575.

Bachant, P., & Wosnik, M. (2015). Characterising the near-wake of a cross-flow turbine. *Journal of Turbulence*, *16*, 392 – 410. doi:10.1080/14685248.2014.1001852.

Bachant, P., & Wosnik, M. (2016). Effects of reynolds number on the energy conversion and near-wake dynamics of a high solidity vertical-axis cross-flow turbine. *Energies*, *9*, 1 – 18. doi:10.3390/en9020073.

Bastankhah, M., & Porté-Agel, F. (2014). A new analytical model for wind-turbine wakes. *Renewable Energy*, *70*, 116 – 123. doi:10.1016/j.renene.2014.01.002.

Battisti, L., Zanne, L., Dell'Anna, S., Dossena, V., Persico, G., & Paradiso, B. (2011). Aerodynamic Measurements on a Vertical Axis Wind Turbine in a Large Scale Wind Tunnel. *Journal of Energy Resources Technology*, *133*, 031201 (9 pp.). doi:10.1115/1.4004360.

Boudreau, M., & Dumas, G. (2016). Vortex Dynamics in the Wake of Three Generic Types of Free-Stream Turbines. In *ISROMAC 2016, International Symposium on Transport Phenomena and Dynamics of Rotating Machinery, Paper F23-1*. Honolulu, Hawaii, USA.

Brochier, G., Fraunie, P., Beguier, C., & Paraschivoiu, I. (1986). Water Channel Experiments of Dynamic stall on Darrieus wind turbine blades. *AIAA Journal of Propulsion and Power*, *2*, 445 – 449. doi:10.2514/3.22927.

Burton, T. (2011). *Wind Energy Handbook*. (2nd ed.). Chichester, New York: Wiley.

Cal, R. B., Lebron, J., Castillo, L., Kang, H. S., & Meneveau, C. (2010). Experimental study of the horizontally averaged flow structure in a model wind-turbine array boundary layer. *Journal of Renewable and Sustainable Energy*, *2*, 013106 (25 pp.). doi:10.1063/1.3289735.

Calaf, M., Meneveau, C., & Meyers, J. (2010). Large eddy simulation study of fully developed wind-turbine array boundary layers. *Physics of Fluids*, *22*, 015110 (16 pp.). doi:10.1063/1.3291077.

CD-Adapco™ (2014). STAR-CCM+® V9 User's Guide. http://www.cd-adapco.com/products/star-ccm.

Chamorro, L. P., Arndt, R. E. A., & Sotiropoulos, F. (2011). Turbulent Flow Properties Around a Staggered Wind Farm. *Boundary-Layer Meteorology*, *141*, 349–367. doi:10.1007/s10546-011-9649-6.

Chamorro, L. P., Arndt, R. E. A., & Sotiropoulos, F. (2012a). Reynolds number dependence of turbulence statistics in the wake of wind turbines. *Wind Energy*, *15*, 733 – 742. doi:10.1002/we.501.

Chamorro, L. P., Guala, M., Arndt, R. E. A., & Sotiropoulos, F. (2012b). On the evolution of turbulent scales in the wake of a wind turbine model. *Journal of Turbulence*, *13*, 1 – 13. doi:10.1080/14685248.2012.697169.

Chamorro, L. P., Hill, C., Morton, S., Ellis, C., Arndt, R. E. A., & Sotiropoulos, F. (2013a). On the interaction between a turbulent open channel flow and an axial-flow turbine. *Journal of Fluid Mechanics*, *716*, 658 – 670. doi:10.1017/jfm.2012.571.

Chamorro, L. P., & Porté-Agel, F. (2009). A Wind-Tunnel Investigation of Wind-Turbine Wakes: Boundary-Layer Turbulence Effects. *Boundary-Layer Meteorology*, *132*, 129 – 149. doi:10.1007/s10546-009-9380-8.

Chamorro, L. P., & Porté-Agel, F. (2010). Effects of Thermal Stability and Incoming Boundary-layer Flow Characteristics on Wind-turbine Wakes: A Wind-tunnel Study. *Boundary-Layer Meteorology*, *136*, 515 – 533. doi:10.1007/s10546-010-9512-1.

Chamorro, L. P., Troolin, D. R., Lee, S.-J., Arndt, R. E. A., & Sotiropoulos, F. (2013b). Three-dimensional flow visualization in the wake of a miniature axial-flow hydrokinetic turbine. *Experiments in Fluids*, *54*, (12 pp.). doi:10.1007/s00348-013-1459-9.

Chatelain, P., Backaert, S., Winckelmans, G., & Kern, S. (2013). Large Eddy Simulation of Wind Turbine Wakes. *Flow, Turbulence and Combustion*, *91*, 587 – 605. doi:10.1007/s10494-013-9474-8.

Chu, C.-R., & Chiang, P.-H. (2014). Turbulence effects on the wake flow and power production of a horizontal-axis wind turbine. *Journal of Wind Engineering and Industrial Aerodynamics*, *124*, 82 – 89. doi:10.1016/j.jweia.2013.11.001.

Dabiri, J. O. (2011). Potential order-of-magnitude enhancement of wind farm power density via counter-rotating vertical-axis wind turbine arrays. *Journal of Renewable and Sustainable Energy*, *3*, 043104 (12 pp.). doi:10.1063/1.3608170.

Dacles-Mariani, J., Kwak, D., & Zilliac, G. (1999). On numerical errors and turbulence modeling in tip vortex flow prediction. *International Journal for Numerical Methods in Fluids*, *30*, 65 – 82. doi:10.1002/(SICI)1097-0363(19990515)30:1<65::AID-FLD839>3.0.CO;2-Y.

Dacles-Mariani, J., Zilliac, G. G., Chow, J. S., & Bradshaw, P. (1995). Numerical/Experimental Study of a Wingtip Vortex in the Near Field. *AIAA Journal*, *33*, 1561 – 1568. doi:10.2514/3.12826.

Dixon, K., Simão Ferreira, C., Hofemann, C., Van Bussel, G., & Van Kuik, G. (2008). A 3d unsteady panel method for vertical axis wind turbines. In *The proceedings of the European Wind Energy Conference & Exhibition EWEC* (pp. 2981 – 2990). Brussels, Belgium.

El-Askary, W., Sakr, I., AbdelSalam, A. M., & Abuhegazy, M. (2017). Modeling of wind turbine wakes under thermally-stratified atmospheric boundary layer. *Journal of Wind Engineering and Industrial Aerodynamics*, *160*, 1 – 15. doi:10.1016/j.jweia.2016.11.001.

Felli, M., Camussi, R., & Di Felice, F. (2011). Mechanisms of evolution of the propeller wake in the transition and far fields. *Journal of Fluid Mechanics*, *682*, 5 – 53. doi:10.1017/jfm.2011.150.

Simão Ferreira, C. J., Hofemann, C., Dixon, K., Van Kuik, G., & Van Bussel, G. (2010). 3D wake dynamics of the VAWT: Experimental and numerical investigation. In *48th AIAA Aerospace Sciences Meeting Including the New Horizons Forum and Aerospace Exposition*. Orlando, FL, United states. doi:10.2514/6.2010-643.

Simão Ferreira, C. J., Kuik, G., Bussel, G., & Scarano, F. (2009). Visualization by PIV of dynamic stall on a vertical axis wind turbine. *Experiments in Fluids*, *46*, 97 – 108. doi:10.1007/s00348-008-0543-z.

Simão Ferreira, C. J., Van Bussel, G., Scarano, F., & Van Kuik, G. (2007). 2D PIV visualization of dynamic stall on a vertical axis wind turbine. In *Collection of Technical Papers - 45th AIAA Aerospace Sciences Meeting* (pp. 16175 – 16190). Reno, NV, United states volume 23.

Simão Ferreira, C. J., Van Bussel, G. J. W., & Van Kuik, G. A. M. (2006). Wind Tunnel Hotwire Measurements, Flow Visualization and Thrust Measurement of a VAWT in Skew. *Journal of Solar Energy Engineering, Transactions of the ASME*, *128*, 487 – 497. doi:10.1115/1.2349550.

Gosselin, R., Dumas, G., & Boudreau, M. (2016). Parametric study of H-Darrieus vertical-axis turbines using CFD simulations. *Journal of Renewable and Sustainable Energy*, *8*, 053301 (22 pp.). doi:10.1063/1.4963240.

Hamilton, N., Kang, H. S., Meneveau, C., & Cal, R. B. (2012). Statistical analysis of kinetic energy entrainment in a model wind turbine array boundary layer. *Journal of Renewable and Sustainable Energy*, *4*, 063105 (19 pp.). doi:10.1063/1.4761921.

Hofemann, C., Simão Ferreira, C. J., Van Bussel, G. J., Van Kuik, G. A. M., Scarano, F., & Dixon, K. R. (2008). 3D Stereo PIV Study of Tip Vortex Evolution on a VAWT. In *The proceedings of the European Wind Energy Conference & Exhibition EWEC*. Brussels, Belgium.

Hu, H., Yang, Z., & Sarkar, P. (2012). Dynamic wind loads and wake characteristics of a wind turbine model in an atmospheric boundary layer wind. *Experiments in Fluids*, *52*, 1277 – 1294. doi:10.1007/s00348-011-1253-5.

Kang, S., Borazjani, I., Colby, J. A., & Sotiropoulos, F. (2012). Numerical simulation of 3D flow past a real-life marine hydrokinetic turbine. *Advances in Water Resources*, *39*, 33 – 43. doi:10.1016/j.advwatres.2011.12.012.

Kazda, J., Zendehbad, M., Jafari, S., Chokani, N., & Abhari, R. (2016). Mitigating adverse wake effects in a wind farm using non-optimum operational conditions. *Journal of Wind Engineering and Industrial Aerodynamics*, *154*, 76 – 83. doi:10.1016/j.jweia.2016.04.004.

Kinsey, T., & Dumas, G. (2012a). Computational fluid dynamics analysis of a hydrokinetic turbine based on oscillating hydrofoils. *Journal of Fluids Engineering*, *134*, 021104 (16 pp.). doi:10.1115/1.4005841.

Kinsey, T., & Dumas, G. (2012b). Three-Dimensional Effects on an Oscillating-Foil Hydrokinetic Turbine. *Journal of Fluids Engineering*, *134*, 071105 (11 pp.). doi:10.1115/1.4006914.

Kinsey, T., & Dumas, G. (2016). Impact of channel blockage on the performance of axial and cross-flow hydrokinetic turbines. *Renewable Energy*, *103*, 239 – 254. doi:10.1016/j.renene.2016.11.021.

Kinzel, M., Araya, D. B., & Dabiri, J. O. (2015). Turbulence in vertical axis wind turbine canopies. *Physics of Fluids*, *27*, 115102 (17 pp.). doi:10.1063/1.4935111.

Kinzel, M., Mulligan, Q., & Dabiri, J. O. (2012). Energy exchange in an array of vertical-axis wind turbines. *Journal of Turbulence*, *13*, 1 – 13. doi:10.1080/14685248.2012.712698.

Kinzel, M., Mulligan, Q., & Dabiri, J. O. (2013). Energy exchange in an array of vertical-axis wind turbines. *Journal of Turbulence*, *14*, 38 – 39. doi:10.1080/14685248.2013.825725.

Klaptocz, V., Crawford, C., Shives, M., Franchini, I., & Mete Sireli, E. (2014). *Impact of channel blockage, free surface proximity and foundations on the performance of Tidal/River Energy Converters*. Technical Report Marine Energy Standards TC114.

Lago, L., Ponta, F., & Chen, L. (2010). Advances and trends in hydrokinetic turbine systems. *Energy for Sustainable Development*, *14*, 287–296. doi:10.1016/j.esd.2010.09.004.

Lebron, J., Castillo, L., & Meneveau, C. (2012). Experimental study of the kinetic energy budget in a wind turbine streamtube. *Journal of Turbulence*, *13*, 1 – 22. doi:10.1080/14685248.2012.705005.

Li, Y., & Calisal, S. M. (2010). Three-dimensional effects and arm effects on modeling a vertical axis tidal current turbine. *Renewable Energy*, *35*, 2325 – 2334. doi:10.1016/j.renene.2010.03.002.

Lignarolo, L. E. M., Ragni, D., Krishnaswami, C., Chen, Q., Simão Ferreira, C. J., & van Bussel, G. J. W. (2014). Experimental analysis of the wake of a horizontal-axis wind-turbine model. *Renewable Energy*, *70*, 31 – 46. doi:10.1016/j.renene.2014.01.020.

Marine Renewables Canada (2014). Marine Renewables Canada (OREG). Http://www.marinerenewables.ca/ (accessed on 2015/01/08).

Medici, D., & Alfredsson, P. H. (2006). Measurements on a wind turbine wake: 3D effects and bluff body vortex shedding. *Wind Energy*, *9*, 219 – 236. doi:10.1002/we.156.

Mehta, D., van Zuijlen, A., Koren, B., Holierhoek, J., & Bijl, H. (2014). Large eddy simulation of wind farm aerodynamics: A review. *Journal of Wind Engineering and Industrial Aerodynamics*, *133*, 1 – 17. doi:10.1016/j.jweia.2014.07.002.

Menter, F. R. (1994). Two-Equation Eddy-Viscosity Turbulence Models for Engineering Applications. *AIAA journal*, *32*, 1598 – 1605. doi:10.2514/3.12149.

Meyers, J., & Meneveau, C. (2013). Flow visualization using momentum and energy transport tubes and applications to turbulent flow in wind farms. *Journal of Fluid Mechanics*, *715*, 335 – 358. doi:10.1017/jfm.2012.523.

Mo, J.-O., Choudhry, A., Arjomandi, M., & Lee, Y.-H. (2013). Large eddy simulation of the wind turbine wake characteristics in the numerical wind tunnel model. *Journal of Wind Engineering and Industrial Aerodynamics*, *112*, 11 – 24. doi:10.1016/j.jweia.2012.09.002.

Mockett, C., Perrin, R., Reimann, T., Braza, M., & Thiele, F. (2010). Analysis of Detached-Eddy Simulation for the Flow Around a Circular Cylinder with Reference to PIV Data. *Flow, Turbulence and Combustion*, *85*, 167 – 180. doi:10.1007/s10494-009-9243-x.

Muscari, R., Di Mascio, A., & Verzicco, R. (2013). Modeling of vortex dynamics in the wake of a marine propeller. *Computers and Fluids*, *73*, 65 – 79. doi:10.1016/j.compfluid.2012.12.003.

Mycek, P., Gaurier, B., Germain, G., Pinon, G., & Rivoalen, E. (2014a). Experimental study of the turbulence intensity effects on marine current turbines behaviour. Part I: One single turbine. *Renewable Energy*, *66*, 729 – 746. doi:10.1016/j.renene.2013.12.036.

Mycek, P., Gaurier, B., Germain, G., Pinon, G., & Rivoalen, E. (2014b). Exper-

imental study of the turbulence intensity effects on marine current turbines behaviour. Part II: Two interacting turbines. *Renewable Energy*, *68*, 876 – 892. doi:10.1016/j.renene.2013.12.048.
Newman, A. J., Drew, D. A., & Castillo, L. (2014). Pseudo spectral analysis of the energy entrainment in a scaled down wind farm. *Renewable Energy*, *70*, 129 – 141. doi:10.1016/j.renene.2014.02.003.
Paraschivoiu, I. (2002). *Wind Turbine Design: With Emphasis on Darrieus Concept*. Polytechnic International Press.
Peng, H., Lam, H., & Lee, C. (2016). Investigation into the wake aerodynamics of a five-straight-bladed vertical axis wind turbine by wind tunnel tests. *Journal of Wind Engineering and Industrial Aerodynamics*, *155*, 23 – 35. doi:10.1016/j.jweia.2016.05.003.
Porté-Agel, F., Wu, Y.-T., Lu, H., & Conzemius, R. J. (2011). Large-eddy simulation of atmospheric boundary layer flow through wind turbines and wind farms. *Journal of Wind Engineering and Industrial Aerodynamics*, *99*, 154 – 168. doi:10.1016/j.jweia.2011.01.011.
Rethore, P.-E. (2009). *Wind Turbine Wake in Atmospheric Turbulence*. Ph.D. thesis Aalborg University Denmark.
Ryan, K. J., Coletti, F., Elkins, C. J., Dabiri, J. O., & Eaton, J. K. (2016). Three-dimensional flow field around and downstream of a subscale model rotating vertical axis wind turbine. *Experiments in Fluids*, *57*, 1 – 15. doi:10.1007/s00348-016-2122-z.
Sanderse, B., van der Pijl, S. P., & Koren, B. (2011). Review of computational fluid dynamics for wind turbine wake aerodynamics. *Wind Energy*, *14*, 799 – 819. doi:10.1002/we.458.
Scheurich, F., Fletcher, T. M., & Brown, R. E. (2011). Simulating the aerodynamic performance and wake dynamics of a vertical-axis wind turbine. *Wind Energy*, *14*, 159 – 77. doi:10.1002/we.409.
Shamsoddin, S., & Porté-Agel, F. (2014). Large eddy simulation of vertical axis wind turbine wakes. *Energies*, *7*, 890 – 912. doi:10.3390/en7020890.
Sherry, M., Nemes, A., Lo Jacono, D., Blackburn, H. M., & Sheridan, J. (2013). The interaction of helical tip and root vortices in a wind turbine wake. *Physics of Fluids*, *25*, 117102 (16 pp.). doi:10.1063/1.4824734.
Shur, M., Spalart, P. R., Strelets, M., & Travin, A. (1999). Detached-eddy simulation of an airfoil at high angle of attack. In *Engineering turbulence modelling and experiments 4, Proceedings of the 4th International Symposium on Engineering Turbulence Modelling and Measurements* (pp. 669–678). Ajaccio, Corsica, France.
Sørensen, J. N. (2011). Aerodynamic Aspects of Wind Energy Conversion. *Annual Review of Fluid Mechanics*, *43*, 427 – 448. doi:10.1146/annurev-fluid-122109-160801.
Spalart, P. R. (2000). Strategies for turbulence modelling and simulations. *International Journal of Heat and Fluid Flow*, *21*, 252 – 263. doi:10.1016/S0142-727X(00)00007-2.
Spalart, P. R. (2001). *Young-Person's Guide to Detached-eddy Simulation Grids*. Technical Report NASA contractor report.
Spalart, P. R. (2009). Detached-Eddy Simulation. *Annual Review of Fluid Mechanics*, *41*, 181–202. doi:10.1146/annurev.fluid.010908.165130.
Spalart, P. R., & Allmaras, S. R. (1994). A one-equation turbulence model for aerodynamic flows. *La Recherche Aérospatiale*, *1*, 5 – 21.
Spalart, P. R., Deck, S., Shur, M. L., Squires, K. D., Strelets, M. K., & Travin, A. (2006). A New Version of Detached-eddy Simulation, Resistant to Ambiguous Grid Densities. *Theoretical and Computational Fluid Dynamics*, *20*, 181–195. doi:10.1007/s00162-006-0015-0.
Spalart, P. R., Jou, W.-H., Strelets, M., & Allmaras, S. R. (1997). Comments on the Feasibility of LES for Wings, and on a Hybrid RANS/LES Approach. In *Advances in DNS/LES, Proceedings of the First AFOSR International Conference on DNS/LES* (pp. 137 – 147). Ruston, Louisiana, USA.
Spalart, P. R., & Rumsey, C. L. (2007). Effective inflow conditions for turbulence models in aerodynamic calculations. *AIAA Journal*, *45*, 2544 – 2553. doi:10.2514/1.29373.
Stevens, R. J., & Meneveau, C. (2017). Flow Structure and Turbulence in Wind Farms. *Annual Review of Fluid Mechanics*, *49*, 311 – 339. doi:10.1146/annurev-fluid-010816-060206.
Tedds, S. C., Owen, I., & Poole, R. J. (2014). Near-wake characteristics of a model horizontal axis tidal stream turbine. *Renewable Energy*, *63*, 222 – 235. doi:10.1016/j.renene.2013.09.011.
Tescione, G., Ragni, D., He, C., Simão Ferreira, C. J., & van Bussel, G. J. W. (2014). Near wake flow analysis of a vertical axis wind turbine by stereoscopic particle image velocimetry. *Renewable Energy*, *70*, 47 – 61. doi:10.1016/j.renene.2014.02.042.
Travin, A., Shur, M., Strelets, M., & Spalart, P. (2002). Physical and Numerical Upgrades in the Detached-Eddy Simulation of Complex Turbulent Flows. In *Advances in LES of Complex Flows* (pp. 239 – 254). volume 65. doi:10.1007/0-306-48383-1_16.
VerHulst, C., & Meneveau, C. (2014). Large eddy simulation study of the kinetic energy entrainment by energetic turbulent flow structures in large wind farms. *Physics of Fluids*, *26*, 025113 (20 pp.). doi:10.1063/1.4865755.
Vermeer, L. J., Sørensen, J. N., & Crespo, A. (2003). Wind turbine wake aerodynamics. *Progress in Aerospace Sciences*, *39*, 467 – 510. doi:10.1016/S0376-0421(03)00078-2.
Wu, Y. T., & Porté-Agel, F. (2012). Atmospheric Turbulence Effects on Wind-Turbine Wakes: an LES study. *Energies*, *5*, 5340 – 62. doi:10.3390/en5125340.
Zhang, W., Markfort, C. D., & Porté-Agel, F. (2012). Near-wake flow structure downwind of a wind turbine in a turbulent boundary layer. *Experiments in Fluids*, *52*, 1219 – 1235. doi:10.1007/s00348-011-1250-8.